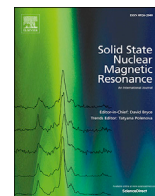




Contents lists available at ScienceDirect

Solid State Nuclear Magnetic Resonance

journal homepage: www.elsevier.com/locate/ssnmr

Broadband adiabatic inversion cross-polarization phenomena in the NMR of rotating solids

Sungsool Wi^{a,*}, Robert W. Schurko^b, Lucio Frydman^{a,c,**}^a National High Magnetic Field Laboratory, Tallahassee, FL, 32304, USA^b Department of Chemistry and Biochemistry, University of Windsor, 401 Sunset Avenue, Windsor, Ontario, NPB 3P4, Canada^c Department of Chemical and Biological Physics, Weizmann Institute of Sciences, Rehovot, 76100, Israel

A B S T R A C T

We explore the use of cross-polarization magic-angle spinning (CPMAS) methods incorporating an adiabatic frequency sweep in a standard Hartman-Hahn CPMAS pulse scheme, to achieve signal enhancements in solid-state NMR spectra of rare spins under fast MAS spinning rates, including spin-1/2, integer spin, and half-integer spin nuclides. These experiments, dubbed Broadband Adiabatic INversion Cross-Polarization Magic-Angle Spinning (BRAIN-CPMAS) experiments, involve an adiabatic inversion pulse on the *S*-channel of a rare spin nuclide while simultaneously applying a conventional spin-locking pulse on the *I*-channel (¹H). The signal enhancement imparted by this CP scheme on the *S*-spin is broadbanded, while employing low RF field strengths on both *I*- and *S*-channels. A feature demanded by these BRAIN-CPMAS methods is to impose a selective adiabatic frequency sweep over a single MAS spinning centerband or sideband, to avoid interference between the MAS modulation and sweeps over multiple sidebands. Upon implementing this swept-CP method, a number of MAS-driven processes happen, including broadband zero- and double-quantum CP transfers, and MAS-driven rotary-resonance phenomena. When this CP method is applied to integer and half-integer quadrupolar nuclei at very fast MAS spinning rates, a favorable double-quantum CP condition is found that can be easily achieved, and avoids the level-crossings among various *m_s* energy levels that complicate quadrupolar CPMAS NMR experiments along lines first shown by Alex Vega. An additional CP mechanism was found in the ¹H-²H case, involving static-like zero-quantum CP modes driven by a quadrupole-modulated RF-dipolar zero-order recoupling under MAS. All these phenomena were examined using average Hamiltonian theory, numerical simulations, and experiments on model compounds. Sensitivity-enhanced, distortion-free CP over wide bandwidths were predicted and observed for *S* = 1/2 and for *S* = 1 (²H) under fast MAS rates. BRAIN-CPMAS also delivered undistorted central transition NMR spectra of half-integer quadrupolar nuclei, while utilizing low RF field strengths that avoid complex level-crossing effects under high MAS rates.

1. Introduction

Solid-state nuclear magnetic resonance (SSNMR) is a powerful tool for characterizing the structures and dynamics of molecules [1–11]. The power of SSNMR stems in part from the development and utilization of cross-polarization magic-angle spinning (CPMAS) methods [12,13] for increasing the signal of the dilute and/or low-gamma nuclei. Under typical spinning speeds and rf fields, conventional CPMAS utilizing rectangular [12,13] or ramped [14] pulses affords spectra from spin-1/2 (¹³C, ¹⁵N, ³¹P) nuclei with significant sensitivity enhancements [15–18]. However, CPMAS requires stringent radiofrequency (rf) field conditions to satisfy the Hartmann-Hahn (HH) matching conditions [19,20], particularly at high *B*₀ fields, where fast spinning rates may be needed to average the large chemical shift anisotropies (CSAs). CPMAS also requires high RF powers to provide efficient polarization transfer over large frequency bandwidths (e.g., to cover large distributions of chemical shifts), which may not be suitable for conducting experiments on

biological samples due to associated heating effects. And while low-power matching conditions can arise in fast-spinning cases, these may fail to allow for polarization transfer over the wide bandwidths necessary for obtaining spectra of rare spin nuclides at high magnetic field strengths, especially those with large chemical shift distributions or broad powder patterns arising from CSA [21,22]. This has stimulated the development of new CPMAS strategies compatible with large spectral bandwidths, fast MAS rates, and moderate RF power levels [23–35]. The search for CPMAS strategies for quadrupolar nuclides is even more challenging, since when dealing with quadrupolar nuclei there are level-crossing effects that lead to periodic, orientation-dependent losses of polarization during its transfer from the high- γ to low- γ nuclei, as first shown by Vega's pioneering work [36].

Frequency-swept RF pulses have long been used in NMR and MRI for achieving inversion of spin polarization, increasing the efficiency of heteronuclear decoupling, or obtaining broadband excitation profiles – in all cases, while allowing for substantial reductions in the magnitude of

* Corresponding author.

** Corresponding author. National High Magnetic Field Laboratory, Tallahassee, FL, 32304, USA.

E-mail addresses: sungsool@magnet.fsu.edu (S. Wi), lucio.frydman@weizmann.ac.il (L. Frydman).<https://doi.org/10.1016/j.ssnmr.2018.08.003>

Received 10 January 2018; Accepted 8 August 2018

Available online 10 August 2018

0926-2040/© 2018 Elsevier Inc. All rights reserved.

the rf powers [37–57]. Additionally, swept pulses are normally very useful in experiments where there is a sensitivity to B_1 -inhomogeneity. The frequency sweep in these pulses is usually implemented in an “adiabatic” mode, where the angle between the spin magnetization and the effective field remains constant [49]. Adiabatic pulse schemes have proven useful for obtaining ultra-wideline NMR spectra of both spin-1/2 and quadrupolar nuclei [58–64]. A broadband cross-polarization (CP) technique, known as broadband-adiabatic inversion-CP (BRAIN-CP) [59] has been developed to cover a broad range of HH matching conditions [19,20], and deliver superior ultra-wideline NMR spectra of rare nuclei under static conditions. Lying at the core of the BRAIN-CP is an adiabatic inversion pulse, which replaces the monochromatic spin-lock pulse on the rare-spin S -channel in conventional CP. This leads to a sequential fulfillment of the HH matching conditions, as the effective strengths of the swept RF pulse on S -nuclei in different crystallite orientations, progressively matches the spin-locking field of the abundant I -nuclei. BRAIN-CP can also be combined with Wideband Uniform-Rate Smooth-Truncation (WURST) based CPMG schemes for further improving the signal-to-noise ratio (SNR) in static NMR spectra, including ultra-wideline applications to ^{119}Sn , ^{195}Pt , ^{199}Hg , ^{39}K , ^{14}N and ^{35}Cl NMR [59,65–67].

While BRAIN-CP was initially developed for obtaining wideline static spectra, it has been recently extended to MAS NMR studies of spin-1/2, 1, and 3/2 nuclides [68–70]. Describing the resulting BRAIN-CPMAS variant, particularly under the $\nu_r \geq 50$ kHz spinning rates that are rapidly becoming routine in SSNMR experiments at high fields, is the aim of the present review. We start by briefly summarizing the behavior of isolated spin $S \geq 1/2$ nuclei ensembles subject to adiabatic inversion pulses in rotating solids. This background material is then used to examine the $I \rightarrow S$ polarization transfer dynamics in spin pairs, upon applying the BRAIN-CPMAS sequence. During these frequency sweeps multiple HH matching conditions arise, including spinning-modulated zero-quantum (ZQ) and double-quantum (DQ) CP modes that may repeatedly occur for a given spin pair over the course of a sufficiently wide frequency sweep. Also observed were novel static-like ZQ matching conditions arising from quadrupolar-driven RF-dipolar recoupling under MAS, as well as hitherto unreported interferences between spin-locking and rotary resonance (RR) phenomena arising from the modulation of even small S -spin shift anisotropies and/or first-order quadrupolar interactions [68,69]. An average Hamiltonian theory was developed to understand these phenomena, and was corroborated by both exact numerical simulations and NMR experiments on model amino acids and on ^{23}Na - and ^{11}B -containing inorganic compounds. Overall, we find that this new CPMAS scheme can deliver polarization from protons to spin-1/2 and to ^2H over a broad range of offsets, under fast MAS rates and using low RF field strengths. BRAIN-CPMAS was also implemented on the central transition (CT) NMR powder patterns of half-integer quadrupolar nuclei [70]; while enhancements were not optimal, the approach led to fewer powder lineshape distortions than afforded by conventional CP techniques while imposing low RF strength requirements.

2. Inversion properties of swept RF pulses: considerations for spin-1/2, 1, and 3/2 ensembles in spinning powders

Before addressing the use of adiabatic inversion pulses in CPMAS pulse sequences, we review the properties of these pulses as applied on isolated S -spin ensembles. In the phase-modulated (PM) frame that corresponds to the usual rotating frame, the Hamiltonian describing this pulse is given by Ref. [37].

$$H_{rf}^s(t) = -\omega_{1s} \cdot A(t) \cdot (S_x \cos \psi(t) + S_y \sin \psi(t)). \quad (1)$$

Here $\omega_{1s} = 2\pi\nu_{1s} = -\gamma_s B_{1s}$ is the maximum field amplitude of the RF field, $A(t)$ is the RF's amplitude envelope, S_x and S_y are the transverse spin angular momentum operators, and $\psi(t)$ is a time-dependent modulation profile. For simplicity we assume that this involves a linear frequency

sweep; i.e.,

$$\psi(t) = \frac{\Delta\omega}{2t_p} t^2 - \frac{\Delta\omega}{2} t + \psi_0, \quad (2)$$

where ψ_0 , $\Delta\omega = 2\pi\Delta\nu$, and t_p are an arbitrary initial phase, the bandwidth of the frequency sweep, and the duration of the pulse, respectively. We also assume a WURST pulse profile where $A(t) = (1 - \cos^{40}[\pi t/t_p])$, even if other amplitude modulation forms could also be considered [37,40,44]. In addition to this interaction, the behavior of the nuclear spins will be influenced by isotropic and anisotropic interactions that depend on their spin number; we consider these as follows.

2.1. Spin-1/2 case

For an isolated spin-1/2 ensemble, the spin Hamiltonian $H_S(t)$ in the PM frame will be

$$H_S(t) = -(\Omega_s + \omega_{\text{CSA}})S_z + H_{rf}^s(t), \quad (3)$$

where $\Omega_s = \omega_0 - \omega_{\text{rf}}$ is the center offset of the sweep, ω_{CSA} is the (eventually MAS-modulated) CSA, and $H_{rf}^s(t)$ is as given in Eq. (1). The spin dynamics imposed by $H_S(t)$ can be conveniently evaluated in a frequency-modulated (FM) frame that is rotating synchronously with the $\psi(t)$ in Eq. (2) [37,40,44]. The spin Hamiltonian in this FM frame, $H_S^{FM}(t)$, can be obtained by

$$H_S^{FM}(t) = UH_S(t)U^{-1} + iU\frac{d}{dt}U^{-1}, \quad (4)$$

where $U = \exp[i\Psi(t)S_z]$. The result is

$$H_S^{FM}(t) = -\left[\Omega_s + \omega_{\text{CSA}} - \frac{d\Psi(t)}{dt}\right]S_z - \omega_{1s}A(t)S_x, \quad (5)$$

where $d\Psi(t)/dt$ is the RF's instantaneous frequency offset given by

$$\frac{d\Psi(t)}{dt} = \omega_p(t) = \frac{\Delta\omega}{t_p} t - \frac{\Delta\omega}{2}, \quad (6)$$

and, except for its isotropic component, the non-secular Coriolis term in Eq. (5) has been ignored. Given a suitable value of ω_{1s} , H_S^{FM} will impose on the S -spin a nutation around an effective axis in the x - z plane of the FM frame. The effective frequency of this nutation will be given by

$$\omega_{\text{eff}}(t) = 2\pi\nu_{\text{eff}}(t) = \sqrt{[\dot{\Omega}_s(t) + \omega_{\text{CSA}}]^2 + [\omega_{1s}A(t)]^2}, \quad (7a)$$

while its inclination vs the z -axis will be

$$\theta = \tan^{-1} [\omega_{1s}A(t) / [\dot{\Omega}_s(t) + \omega_{\text{CSA}}]] \quad (7b)$$

where $\dot{\Omega}_s(t) = \Omega_s - \omega_p(t)$. Notice that in the absence of CSA, Eq. (7) predicts that a sweep of ω_p through the on-resonance Ω_s frequency under the action of a suitable amplitude of ω_{1s} will transform a magnetization that was initially $+S_z$ into a $-S_z$ state; this lies at the origin of the well-known inversion operation associated with swept adiabatic passages [37,40,44].

We consider next the behavior of this $S = 1/2$ site under the action of MAS at a rate $\omega_r = 2\pi\nu_r$. This can be accounted for by imparting the CSA in Eq. (5) with a time dependence $\omega_{\text{CSA}}(t) = \sum_{k=-2}^2 a_k e^{ik\omega_r t} S_z$, where the $\{a_k(\delta_{\text{CSA}}, \eta)\}$ coefficients have the usual dependence on the Euler angle set transforming the tensor parameters δ_{CSA} and η (defined in the CSA's principal axis system) into the rotor frame [71]. Shown in Fig. 1 are simulated inversion profiles for an initial state $+S_z$, arising for an on-resonance sweep for different WURST pulse sweep widths, $\Delta\nu$. The inversion behavior is unlike that observed for a static solid or liquid in that, even for narrowband $\Delta\nu < \nu_r$ sweeps, S_z inverts not only around the

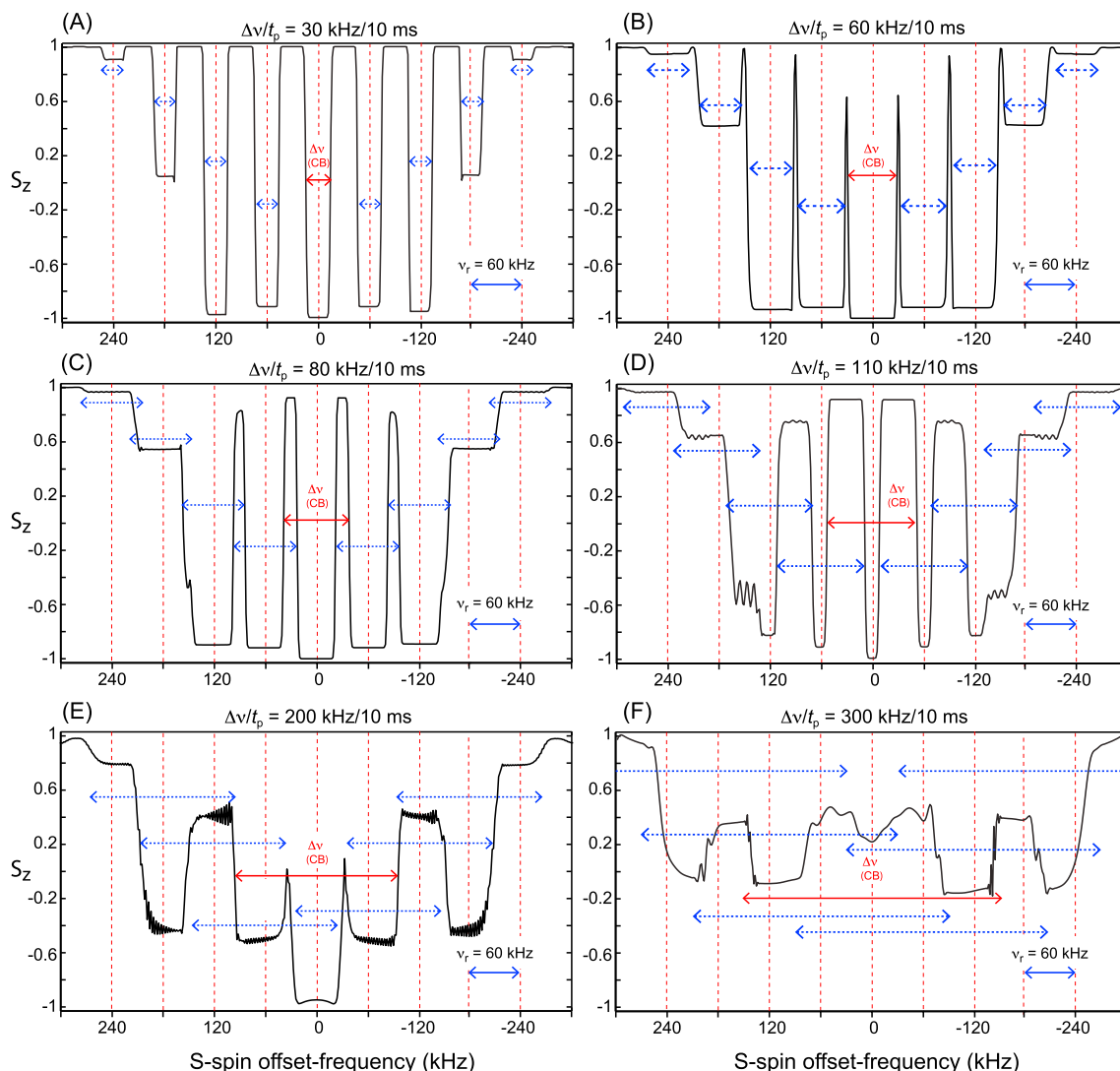


Fig. 1. S_z inversion profiles calculated upon varying the span $\Delta\nu$ of a WURST pulse for an anisotropic site under a MAS rate $\nu_r = 60$ kHz. An isolated ensemble of spin-1/2 nuclei ($\delta_{\text{CSA}} = 400$ ppm, $\eta = 1$, $\nu_0 = 150$ MHz) irradiated at on-resonance by an RF field of $\nu_{1S} = 20$ kHz, was considered. $\Delta\nu$ was varied as 30 (A), 60 (B), 80 (C), 110 (D), 200 (E), and 300 kHz (F), always for a $t_p = 10$ ms sweep pulse length. Dashed vertical lines indicate the positions of the site's centerband (CB) and spinning sidebands. The red central double arrow ($\Delta\nu$, CB) refers to the actual extent of the sweeps; horizontal blue arrows are virtual replicas centered at off-resonance positions separated by the spinning rate. Notice the differences arising when $\Delta\nu$ is chosen to be smaller than ν_r ; the shape and width of the inversion profile are identical to the isotropic S_z state expectation within the center-sweep region (A,B); the maximum width of the inversion profile is achieved when $\Delta\nu = \nu_r$ (B). When $\nu_r > \Delta\nu > 2\nu_r$, interferences occur between the center and sideband inversion profiles, resulting in the decrease of the successfully inverted central region (C and D). When $\Delta\nu \gg 2\nu_r$, the frequency regions of interference exceed the $|2\nu_r|$ window, resulting in the disappearance of S_z 's central inversion profile (E and F). (For interpretation of the references to color in this figure legend, the reader is referred to the Web version of this article.)

centerband (the center of which is “touched” by the sweep), but also around the sideband frequency positions separated by $\pm\nu_r$, $\pm 2\nu_r$ etc. The inversion is thus split into multiple “bands”, the frequency width of which is identical to the RF sweep bandwidth $\Delta\nu$ –as long as the sweep width regions of the center- and side-bands do not overlap. The maximum inversion bandwidth is thus obtained for $\Delta\nu = \nu_r$ (Fig. 1B). If $\nu_r < \Delta\nu < 2\nu_r$, the inversion bandwidth of the centerband overlaps with those from the neighboring sidebands, resulting in a narrower inversion profile at the centerband due to destructive interferences (Fig. 1C and D). When $\Delta\nu \geq 2\nu_r$, sweeps at frequency bands positioned at multiple $n\nu_r$ harmonics ($n = 0, \pm 1, \pm 2, \dots$) interfere with one another, and eventually the possibility of obtaining fully inverted S_z along the centerband is lost (Fig. 1E and F).

2.2. Spin-1 case

We focus next on the spin dynamics occurring when these waveforms

are applied to a spin-1 nucleus such as ^2H , for which quadrupolar effects are suitably addressed by a first perturbative term. The spin Hamiltonian for these nuclei in the FM frame becomes

$$H_S^{FM}(t) = -[\Omega_S^2(t) + \omega_{\text{CSA}}(t)]S_z - \omega_{1s}A(t)S_x + H_{QS}^{(1)}(t), \quad (8)$$

where the terms and parameters are as in Eq. (3), except for a first-order quadrupolar interaction $H_Q^{(1)}(t)$ that under MAS is given by Ref. [72].

$$H_{QS}^{(1)}(t) = \chi_Q \omega_Q(t) [3S_z^2 - S(S+1)], \quad (9)$$

with $\chi_Q = C_Q/2S(2S-1) = e^2qQ/2S(2S-1)\hbar$,

$$\omega_Q(t) = \frac{1}{8} \sin^2\beta \cos(2\omega_r t + 2\gamma) - \frac{1}{4\sqrt{2}} \sin 2\beta \cos(\omega_r t + \gamma) \quad (10)$$

the usual quadrupole coupling parameters, and the asymmetry parameter

η_Q assumed to be zero [73]. The dominant first-order quadrupolar term $H_Q^{(1)}(t)$ can be removed by transforming Eq. (8) into a quadrupolar interaction frame according to

$$\tilde{H} = U_Q H_S^{FM}(t) U_Q^{-1} + i(dU_Q^{-1}/dt)U_Q, \quad (11)$$

where

$$U_Q = T \exp \left\{ i \int_0^t \chi_Q \omega_Q(t') dt' (3S_z^2 - 2) \right\} \quad (12)$$

with T the Dyson time-ordering operator. When Eq. (11) is integrated over a powder, the γ -angle averaged Coriolis term, $\langle i(dU_Q^{-1}/dt)U_Q \rangle_\gamma$,

vanishes [74]. Since all terms in Eq. (8), with an exception of the RF Hamiltonian, commute with $H_Q^{(1)}(t)$ at all times, only the RF Hamiltonian is modified by transforming into this quadrupolar interaction frame. Then, the RF Hamiltonian in this frame is given as:

$$\begin{aligned} \tilde{H}_{rf}(t) = & -\omega_{1S} \left\{ S_x \cos \left(\int_0^t 3\chi_Q \omega_Q(t') dt' \right) + [S_y S_z \right. \\ & \left. + S_z S_y] \sin \left(\int_0^t 3\chi_Q \omega_Q(t') dt' \right) \right\}. \end{aligned} \quad (13)$$

The spin-locking behavior of the S -spin polarization is dramatically changed by these time dependencies vis-à-vis its spin-1/2 counterpart, as first described in A. Vega's pioneering work [75]. As he taught us, the fate

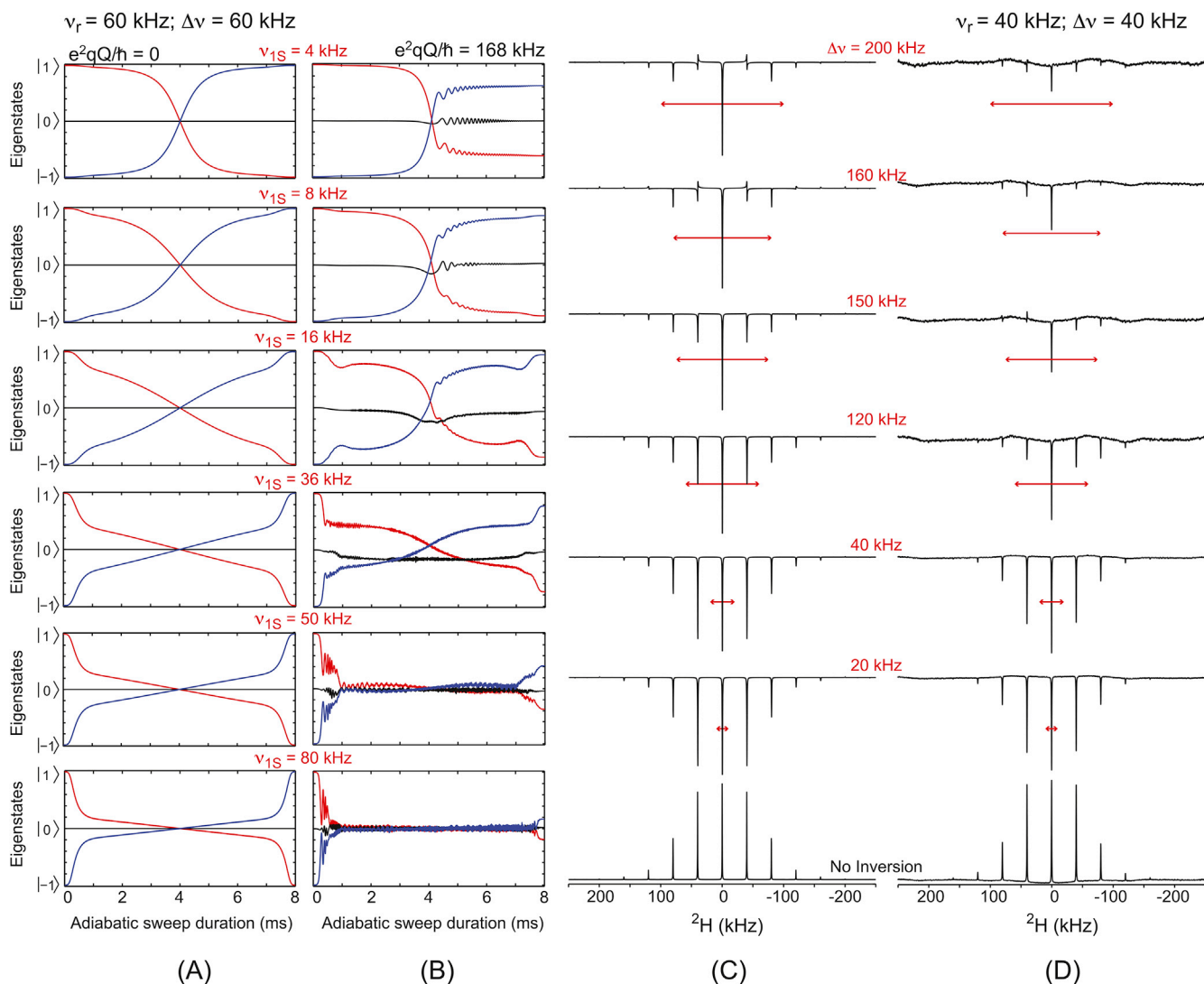


Fig. 2. Inversion properties among energy levels $|1\rangle$, $|0\rangle$ and $|-1\rangle$ (shown in red, black and blue respectively) of a spin-1 powder under a WURST-40 sweep without (A) and with (B) considering a quadrupolar coupling parameter $C_Q = e^2qQ/h = 168$ kHz and a MAS spinning rate $\nu_r = 60$ kHz. The CSA assumed in all simulations was $\delta_{csa} = 921$ Hz (10 ppm at 14.1T), and both quadrupolar and shielding tensors were assumed to be collinear and have null asymmetries ($\eta = 0$). The WURST pulse parameters utilized were: $\Delta\nu = \nu_r$; $t_p = 8$ ms, pulse power ν_{1S} varied from 4 kHz to 80 kHz as indicated in the figure. No significant differences arise between (A) and (B) when ν_{1S} is small (<16 kHz), hinting at the optimal ν_{1S} value that can be used for performing a nearly ideal ^2H adiabatic inversion. Shown in (C) and (D) simulated and experimental inversion spectra obtained for d_2 -2,2-glycine ($C_Q = 168$ kHz; $\nu_0 = 92.1$ MHz) upon variation of the $\Delta\nu$ of the WURST pulse applied on-resonance under MAS spinning rate $\nu_r = 40$ kHz. All experiments were done on a methylene-deuterated glycine sample at 14.1 T and used a strong 90-degree read pulse directly before detection. The free evolution was digitized for 8.192 ms (data points: 4096; dwell time: 2 μs) and Fourier transformed to yield the spectra. The magnitudes of $\Delta\nu$ are indicated in the middle of the figure, and the breadths of the sweeps are illustrated by red, horizontal, arrowed lines. All pulses were swept for $t_p = 8$ ms with $\nu_{1S} = 8$ kHz. The spectra shown on the bottom of both columns are simulated and experimental MAS spectra obtained without inversion. (For interpretation of the references to color in this figure legend, the reader is referred to the Web version of this article.)

of a spin-locked magnetization can be evaluated by inspecting the adiabaticity parameter $\alpha = \frac{\omega_{1S}^2}{\chi_Q \omega_r}$, which specifies the nature of the level-crossings induced by the RF describing whether the passage is sufficiently fast to be sudden, sufficiently slow to be adiabatic, or intermediate [75]. When $\alpha = \frac{\omega_{1S}^2}{\chi_Q \omega_r} \ll 1$ the system is said to be in the sudden passage regime; under these conditions, the RF does not cause population redistributions among different levels because the $|1\rangle$, $|0\rangle$, and $|-1\rangle$ levels are maintained as eigenstates during the course of the spin-locking period. For prototypical ^2H sites (e.g., $C_Q = 168$ kHz) and the fast ($\nu_r \geq 40$ kHz) spinning rates conditions here considered, easily achievable ν_{1S} rf fields fulfill this sudden-passage regime (Fig. 2). In this regime, only the term

$$\tilde{H}_{rf}(t) \approx -\omega_{1S}A(t)S_x \cos\left(\int_0^t 3\chi_Q \omega_Q(t') dt'\right) \quad (14)$$

needs then to be considered. Employing a matrix representation, Eq. (8) can then be explicitly written as

$$\tilde{H}_S^{FM}(t) =$$

$$\begin{bmatrix} -\Omega_S^i(t) - \omega_{CSA}(t) & -\frac{\omega_{1S}}{\sqrt{2}}A(t)S_x \cos\left(\int_0^t 3\chi_Q \omega_Q(t') dt'\right) & 0 \\ -\frac{\omega_{1S}}{\sqrt{2}}A(t)S_x \cos\left(\int_0^t 3\chi_Q \omega_Q(t') dt'\right) & 0 & -\frac{\omega_{1S}}{\sqrt{2}}A(t)S_x \cos\left(\int_0^t 3\chi_Q \omega_Q(t') dt'\right) \\ 0 & -\frac{\omega_{1S}}{\sqrt{2}}A(t)S_x \cos\left(\int_0^t 3\chi_Q \omega_Q(t') dt'\right) & \Omega_S^i(t) + \omega_{CSA}(t) \end{bmatrix}. \quad (15)$$

This matrix can be separated into two terms related solely to the $|1\rangle \leftrightarrow |0\rangle$ and $|0\rangle \leftrightarrow |-1\rangle$ single-quantum transition subspaces:

$$\tilde{H}_S^{FM}(t) = \begin{bmatrix} -\Omega_S^i(t) - \omega_{CSA}(t) & -\frac{\omega_{1S}}{\sqrt{2}}A(t)S_x \cos\left(\int_0^t 3\chi_Q \omega_Q(t') dt'\right) & 0 \\ -\frac{\omega_{1S}}{\sqrt{2}}A(t)S_x \cos\left(\int_0^t 3\chi_Q \omega_Q(t') dt'\right) & \Omega_S^i + \omega_{CSA}(t) & 0 \\ 0 & 0 & 0 \end{bmatrix} + \begin{bmatrix} 0 & 0 & 0 \\ 0 & -\Omega_S^i - \omega_{CSA}(t) & -\frac{\omega_{1S}}{\sqrt{2}}A(t)S_x \cos\left(\int_0^t 3\chi_Q \omega_Q(t') dt'\right) \\ 0 & -\frac{\omega_{1S}}{\sqrt{2}}A(t)S_x \cos\left(\int_0^t 3\chi_Q \omega_Q(t') dt'\right) & \Omega_S^i(t) + \omega_{CSA}(t) \end{bmatrix}. \quad (16)$$

These identical expressions for the $|1\rangle \leftrightarrow |0\rangle$ and $|0\rangle \leftrightarrow |-1\rangle$ subspaces can be expressed using a basis of spin- $1/2$ operators:

$$\tilde{H}_S^{FM}(t) = -2[\Omega_S^i(t) + \omega_{CSA}(t)]S_z^{1/2} - \sqrt{2}\omega_{1S}A(t)S_x^{1/2} \cos\left(\int_0^t 3\chi_Q \omega_Q(t') dt'\right). \quad (17)$$

Defining $S_z = 2S_z^{1/2}$ and $S_x = \sqrt{2}S_x^{1/2}$ as fictitious spin- $1/2$ operators possessing the same coefficients as the original spin-1 angular momentum operators, Eq. (17) becomes

$$\tilde{H}_S^{FM}(t) = -[\Omega_S^i(t) + \omega_{CSA}(t)]S_z - \omega_{1S}A(t)S_x \cos\left(\int_0^t 3\chi_Q \omega_Q(t') dt'\right). \quad (18)$$

This is a similar expression as that given for a spin-1/2 nucleus, but for an RF-field that is now modulated by an additional quadrupolar oscillation. It follows from Eq. (18) that a suitable value of ω_{1S} can lead to the inversion of an initial $+S_z$ state, via a $+S_z \rightarrow +S_x \rightarrow -S_z$ FM-frame trajectory similar to that of the spin-1/2 case. The effective nutation frequency of this process is

$$\omega_{eS} = 2\pi\nu_{eS} = \sqrt{\left[\Omega'_S(t) + \omega_{CSA}(t)\right]^2 + \left[\omega_{1S}A(t)\cos\left(\int_0^t 3\chi_Q\omega_Q(t')dt'\right)\right]^2}. \quad (19)$$

Fig. 2A and B displays the inversion properties of a spin-1 manifold during the course of these adiabatic sweeps for different maximum RF amplitudes, with and without a quadrupolar interaction. For a WURST pulse centered on-resonance and spanning a frequency range $\Delta\nu$ (usually $\Delta\nu \leq \nu_r$), $|1\rangle$ and $|-1\rangle$ populations are inverted at the completion of the sweep for all of the ν_{1s} values considered – provided that $C_Q = 0$ kHz. However, when C_Q is assigned a typical value associated with an organic C-²H bond (i.e., $C_Q = 168$ kHz; $\eta_Q = 0$), smooth inversions without level crossings are only observed for low ($\leq \nu_r/2$) RF-pulse amplitudes. By contrast, larger ν_{1s} values introduce fast oscillations among the populations in the $|1\rangle$, $|0\rangle$, and $|-1\rangle$ eigenstates,¹ leading to C_Q - and MAS-driven non-adiabatic transfers among them [75,76]. Inclusion of moderate CSAs (e.g., 10 ppm at 14 T) have no discernible influence on the behavior of S_z for any of the pure Zeeman states, while the effect of MAS on a CSA-only spin-1 is as described for a CSA-bearing spin-1/2 case.

This behavior was investigated by comparing simulated (Fig. 2C) and experimental (Fig. 2D) ²H MAS spectra [77–80]; the latter acquired by first applying a WURST inversion pulse with varying $\Delta\nu$, followed by a strong $\pi/2$ “read” pulse for detection. Also shown at the bottom of each column are the MAS lineshapes obtained/expected at $\nu_r = 40$ kHz. When the swept pulse bandwidth $\Delta\nu < 2\nu_r$, simulated and experimental spectra are similar: they are distortion-free, and completely inverted. However, when $\Delta\nu > 2\nu_r$, the simulated and experimental spectra differ: lineshapes are distorted and there are decreased relative intensities among the spinning sidebands. Finally, if $\Delta\nu > 3\nu_r$, severely phase-distorted MAS spectra result from multiple interferences between the centerband and the sidebands as the adiabatic sweep proceeds. This is akin to what has been reported for $S = 1/2$ cases [68,77–80], and to what is shown in Fig. 1. This behavior suggests limits for the sweep widths that can be applied in BRAIN-CPMAS experiments on quadrupolar nuclides.

2.3. Spin-3/2 case

The application of swept adiabatic inversion pulses on half-integer quadrupolar spins, has been previously considered [81–84]. We revisit this problem by considering the FM-frame Hamiltonian of an ensemble of isolated half-integer ($S \geq 3/2$) nuclei undergoing MAS, on which a frequency-swept pulse is applied

$$H_S^{FM}(t) = \Omega'_S(t)S_z + H_{Q,S}^{(1)}(t) + H_{Q,S}^{(2)}(t) - \omega_{1S}A(t)S_x. \quad (20)$$

Here, $H_{Q,S}^{(1)}(t)$ is the first-order quadrupolar interaction defined as in Eq. (9) and $H_{Q,S}^{(2)}(t)$ represents the second-order quadrupolar interaction defined by

$$H_{Q,S}^{(2)}(t) = \frac{3\chi_Q^2}{\omega_{0,S}} \left[R_{2,-1}^Q(t)R_{2,1}^Q(t)S_z\{4S(S+1) - 8S_z^2 - 1\} + R_{2,-2}^Q(t)R_{2,2}^Q(t)S_z\{2S(S+1) - 2S_z^2 - 1\} \right] \quad (21)$$

The explicit expressions for $R_{2,m}^Q(t)$ ($m = 0, \pm 1, \pm 2$) under MAS are obtained by the usual transformation of the electric-field gradient (EFG) tensor from its principal axis system (PAS) to the rotor frame as given by α_Q , β_Q , and γ_Q Euler angles [85]. Eq. (20) can be rewritten utilizing fictitious spin-1/2 operators [86,87] as

$$H_S^{FM}(t) = H_\Omega(t) + H_{Q,S}^{(1)}(t) + H_{Q,S}^{(2)}(t) \quad (22)$$

where $H_\Omega(t)$ is a shift-like Hamiltonian that consists of the chemical shift, the instantaneous offset frequency $\omega_p(t)$, and the second-order quadrupolar interaction. This can be written as

$$H_\Omega(t) = \left\{ \Omega'_S(t) + \Omega_{Q,S}^{2-3}(t) \right\} S_z^{2-3} + \left\{ 3\Omega'_S(t) + \Omega_{Q,S}^{1-4}(t) \right\} S_z^{1-4}, \quad (23)$$

where S_z^{2-3} and S_z^{1-4} are operators associated with the central (CT) and the triple-quantum (TQ) transitions respectively, and $\Omega_{Q,S}^{2-3}(t)$ and $\Omega_{Q,S}^{1-4}(t)$ represent the second-order quadrupolar interactions for these transitions. The Hamiltonians for the first-order quadrupolar interaction and the RF in Eq. (22) can also be expressed by this fictitious spin-1/2 formalism as

$$H_{Q,S}^{(1)}(t) = \omega_Q(t) \{ S_z^{1-2} - S_z^{3-4} \} \quad (24)$$

and

$$H_{Q,S}^{(2)}(t) = \omega_{1S}A(t) \left\{ 2S_x^{2-3} + \sqrt{3} (S_x^{1-2} + S_x^{3-4}) \right\}. \quad (25)$$

The explicit expressions for $\omega_Q(t)$ and $\Omega_{Q,S}^{m-n}(t)$ ($m-n = 2-3$ and $1-4$) appearing in Eqs. (23) and (24) can be found in our previous publication [70]. Notice that multiple operators are associated with the RF Hamiltonian in Eq. (25): S_x^{2-3} for the CT, and S_x^{1-2} and S_x^{3-4} for the two satellite transitions (STs) – the latter enabling interconversions between CT coherences (CTCs) and triple-quantum coherences (TQCs). To better describe these CTC-TQC conversions we consider Eqs. (24) and (25) in a tilted frame that is rotated by an angle θ defined by Ref. [86].

$$\theta = \tan^{-1} \left[\sqrt{3} \omega_{1S} / \omega_Q(t) \right]. \quad (26)$$

This tilted frame is characterized by an effective RF field, $\omega_e(t)$, described by

$$\sqrt{\omega_Q^2(t) + 3\omega_{1S}^2 A(t)^2} = \omega_e(t). \quad (27)$$

Then, it is possible to transform Eqs. (23)–(25) into this tilted frame by applying a unitary transformation specified by $e^{-i\theta S_y^{1-2}}$ and $e^{i\theta S_y^{3-4}}$ operators, resulting in:

$$H_T = \omega_e (S_z^{1-2} - S_z^{3-4}) + \left\{ \Omega'(t) + \Omega_{Q,S}^{2-3}(t) \right\} \left[\cos^2 \frac{\theta}{2} S_z^{2-3} + 2\sin\theta S_y^{1-2} - \sin^2 \frac{\theta}{2} S_y^{3-4} \right] + \left\{ 3\Omega'(t) + \Omega_{Q,S}^{1-4}(t) \right\} \left[\cos^2 \frac{\theta}{2} S_z^{1-4} + 2\sin\theta S_y^{1-2} - \sin^2 \frac{\theta}{2} S_y^{3-4} \right] + 2\omega_{1S}A(t) \left[\cos^2 \frac{\theta}{2} S_x^{2-3} - \sin^2 \frac{\theta}{2} S_x^{1-4} + 2\sin\theta S_x^{1-3} - 2\sin\theta S_x^{2-4} \right]. \quad (28)$$

The RF term in Eq. (28) now contains the S_x^{2-3} and S_x^{1-4} operators that can excite the CTC and TQC, respectively, as well as S_x^{1-3} and S_x^{2-4} operators that excite double-quantum coherences (DQCs). The magnitude of θ , and thus the magnitude of the applied ω_{1S} under a given $\omega_Q(t)$, must be large in order to excite these DQCs and TQC to an appreciable degree. Notice that all of the S_x^{2-3} , S_x^{1-4} , S_x^{1-3} , and S_x^{2-4} terms in Eq. (28) are modulated by MAS-driven quadrupolar oscillations; therefore, numerical evaluations are generally required for their explicit analysis.

As in the case of spin-1, the evolution imparted by the dominant first-order quadrupolar term, the leading term in this expression, can be removed from Eq. (28) by transforming into a quadrupolar interaction frame defined by

$$\widetilde{H}_T = U_Q H U_Q^{-1} + iU_Q \frac{d}{dt} U_Q^{-1}, \quad (29)$$

¹ For adequately describing this level-crossing effect an assumption made for the sudden passage regime does not apply, and Eq. (13) must be utilized without any approximation.

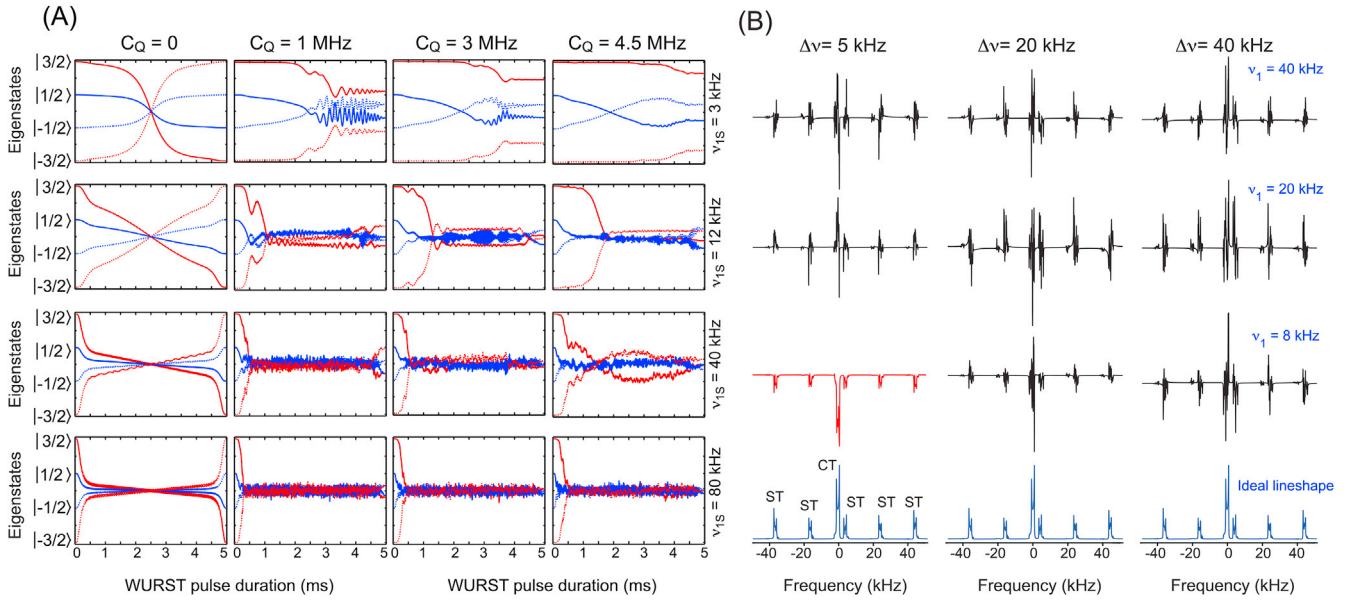


Fig. 3. (A) Inversion and spin-locking properties exhibited by the S_z -states of a spin-3/2 powdered ensemble under the action of a WURST frequency-swept pulse. Simulations are presented for different quadrupolar couplings ($e^2qQ/\hbar = 0, 1, 3,$ and 4.5 MHz) with $\eta_Q = 0$, $\nu_0 = 160.4$ MHz, and different WURST pulse powers ($\nu_{1S} = 3, 12, 40$ and 80 kHz); but for all cases $\Delta\nu = 10$ kHz and $t_p = 5$ ms. The MAS spinning rate ν_r is 40 kHz, and CSA parameters are set to zero for simplicity. (B) Powder simulations for a quadrupolar $S = 3/2$ site ($C_Q = 3$ kHz and $\eta_Q = 0$; $\delta_{iso} = \delta_{CSA} = 0$; $\nu_0 = 160.4$ MHz) under MAS conditions ($\nu_r = 40$ kHz), upon varying the sweep range $\Delta\nu$ and maximum field ν_{1S} of a $t_p = 8$ ms WURST adiabatic inversion pulse. For all simulations, an ideal 90° pulse was applied after the adiabatic sweep, followed by a free evolution digitization over 8.192 ms (4096 data points; $2 \mu\text{s}$ dwell time) and Fourier transform to yield the spectra. The bottom row shows the ideal non-inverted MAS spectrum, denoting the single-quantum central transition (CT) without sidebands, as well as the single-quantum satellite transitions (STs) with visible spinning sidebands. A nearly ideal inversion spectrum of CT and ST (highlighted in red) is obtained only when a narrow $\Delta\nu$ (5 kHz), which does not overlap with any ST sideband(s), is applied with a low ν_{1S} value (8 kHz). (For interpretation of the references to color in this figure legend, the reader is referred to the Web version of this article.)

where $U_Q = \text{Texp}\left\{i \int_0^t dt' \omega_e(t') [S_z^{1-2} - S_z^{3-4}]\right\}$ and $U_{Q\frac{d}{dt}} U_Q^{-1} = 0$. Since the S_z^{2-3} and S_z^{1-4} operators in the shift-like Hamiltonians and the S_x^{2-3} , S_x^{1-4} , S_x^{1-3} , and S_x^{2-4} operators in the RF Hamiltonians commute with S_z^{1-2} and S_z^{3-4} in $H_Q^{(1)}(t)$, this quadrupolar-interaction frame Hamiltonian can be rewritten as

$$\begin{aligned} \widetilde{H}_T = & \left\{ \Omega'(t) + \Omega_{Q,S}^{2-3}(t) \right\} \left[\cos^2 \frac{\theta}{2} S_z^{2-3} + \left\{ 2 \sin \theta S_y^{1-2} - \sin \frac{\theta}{2} S_y^{3-4} \right\} \cos \int_0^t \omega_e(t') dt' \right. \\ & \left. - \left\{ 2 \sin \theta S_x^{1-2} - \sin \frac{\theta}{2} S_x^{3-4} \right\} \sin \int_0^t \omega_e(t') dt' \right] + \left\{ 3 \Omega'(t) \right. \\ & \left. + \Omega_{Q,S}^{1-4}(t) \right\} \left[\cos^2 \frac{\theta}{2} S_z^{1-4} + \left\{ 2 \sin \theta S_y^{1-2} - \sin \frac{\theta}{2} S_y^{3-4} \right\} \cos \int_0^t \omega_e(t') dt' \right. \\ & \left. - \left\{ 2 \sin \theta S_x^{1-2} - \sin \frac{\theta}{2} S_x^{3-4} \right\} \sin \int_0^t \omega_e(t') dt' \right] + \\ & 2\omega_{1S} A(t) \left[\cos^2 \frac{\theta}{2} S_x^{2-3} - \sin^2 \frac{\theta}{2} S_x^{1-4} + 2 \sin \theta S_x^{1-3} - 2 \sin \theta S_x^{2-4} \right]. \end{aligned} \quad (30)$$

Under the condition $\omega_Q \gg \omega_{1S}$, we can approximate $\theta \approx 0$ and $\omega_e \approx \omega_Q$. Then, by considering only the CTC, Eq. (30) reduces to

$$\widetilde{H}_T = \left\{ \Omega'(t) + \Omega_{Q,S}^{2-3}(t) \right\} S_z^{2-3} + 2\omega_{1S} A(t) S_x^{2-3}. \quad (31)$$

Eq. (31) reveals that the RF term for the excitation of the CTC is free from the quadrupolar-induced evolution if $\omega_Q \gg \omega_{1S}$.

Fig. 3A shows the behavior of $S_z = |3/2\rangle, |1/2\rangle, |-1/2\rangle$ and $|-3/2\rangle$ populations when subjected to a WURST-40 pulse as the RF maximum amplitude $\nu_{1S} = \omega_{1S}/2\pi$ and the magnitude of C_Q are varied (again, CSA is ignored for simplicity). For all of the ν_{1S} values considered, $|3/2\rangle, |1/2\rangle, |-1/2\rangle$ and $|-3/2\rangle$ populations are inverted at the completion of the sweep when $C_Q = 0$. However, when $C_Q \neq 0$, level crossings occur during the pulse between the Zeeman eigenstates that are being modulated by MAS-driven quadrupolar oscillations. In accordance to Vega's explanation [75,76], this leads to a rapid dissipation of the spin-locked states, particularly when larger ν_{1S} values are used. Smooth inversions of the CT spectra are achieved only for weak (< 10 kHz) RF amplitudes, for which population inversions occur only between the central $|1/2\rangle$ and $|-1/2\rangle$ eigenstates in accordance with Eq. (31), while changes in populations of the outer $|3/2\rangle$ and $|-3/2\rangle$ energy eigenstates populations are minimal. This suggests that these are the only RF amplitudes suitable for an efficient $I(^1\text{H}) \rightarrow S(\text{CT}; S = 3/2)$ BRAIN-CPMAS signal transfer (*vide infra*).

The behavior of S_z for an ensemble of spin-3/2 nuclei subjected to a WURST-40 pulse was also examined for a powdered sample under 40 kHz MAS. Fig. 3B compares simulated spectra for a single site with $C_Q = 3$ MHz, $\eta_Q = 0$, and $\delta_{CSA} = 0$ ppm (^{11}B @ 11.7 T), upon varying both the amplitude $\nu_{1S} = \omega_{1S}/2\pi$ and the sweep range $\Delta\nu = \Delta\omega/2\pi$ of the WURST pulse. This pulse was assumed followed by an infinitely strong “read pulse”, and by a period of concurrent free evolution and signal digitization. The center of the pulse's sweep range is matched to the center of the central transition peak; i.e., to its isotropic second-order quadrupolar shift [88,89]. Under narrow-sweep, weak-RF conditions ($\Delta\nu = \text{kHz}$, $\nu_{1S} = 8$ kHz), the simulation shows a completely inverted, nearly distortion-free, MAS-averaged, second-order quadrupolar spectrum (marked red in Fig. 3B). However the CT lineshape becomes remarkably distorted if the magnitude of $\Delta\nu > 5$ kHz or if stronger RF fields are applied. This is different from the inversion characteristics

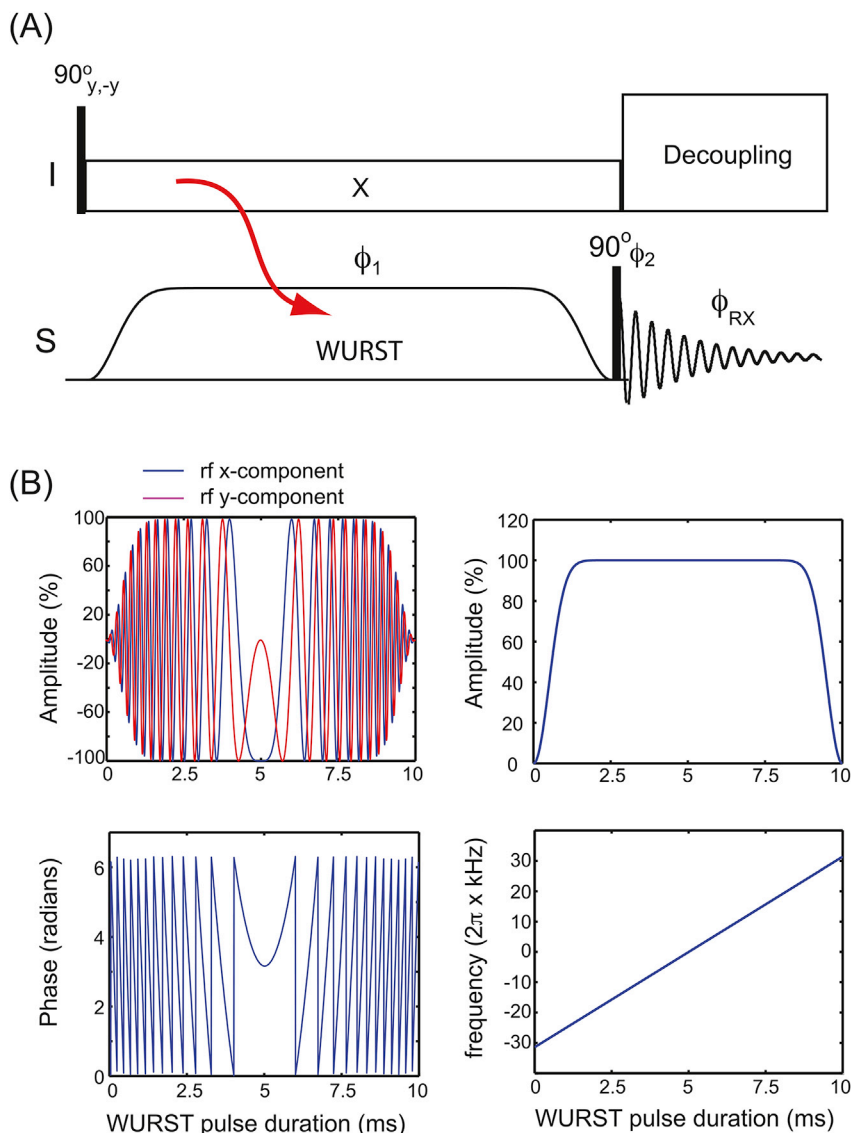


Fig. 4. (A) BRAIN-CPMAS scheme including a phase-modulated WURST pulse applied along the S -channel together with a standard spin-lock I scheme. A 90° “read” pulse is required after the CP mixing time to convert the S_z -polarization obtained from the CP process into detectable signal and I -decoupling is applied during the signal detection. The pulse phases used in the sequence were: $\phi_1 = x, x, y, y, -x, -x, -y, -y$; $\phi_2 = y, y, -x, -x, -y, -y, x, x$; $\phi_{RX} = x, -x, y, -y, -x, x, -y, y$. Illustrated in (B) are the x- (blue) and y-components (red), modulation phase [$\nu(t)$], pulse amplitude given as $\omega_{1S}(1 - \cos^{40}[\pi t/t_p])$, and instantaneous frequency [$d\Psi(t)/dt$] of the RF-field – all for parameters $\Delta\nu = 10$ kHz, $t_p = 10$ ms, and $\Psi_0 = 0^\circ$. (For interpretation of the references to color in this figure legend, the reader is referred to the Web version of this article.)

reported for $S = 1/2$ or small- $C_Q S = 1$ nuclides, for which ideal inversion characteristics were observed for weak ν_{1S} as long as the $\Delta\nu \leq 2\nu_r$ [68, 69]. In the current case, an inverted, undistorted spectrum is only obtained if the $\Delta\nu$ is narrow enough to encompass the breadth of the anisotropic centerband of the CT transition, but does not overlap with the neighboring spinning sidebands of the satellite transitions (STs); by contrast, if both the CT and ST sidebands are traversed by the same RF sweep, clear distortions emerge.

3. Analytical description of BRAIN-CPMAS NMR under a frequency-swept S -pulse

Figs. 1–3 provide means for analyzing the capabilities and the limits of adiabatic sweeps for obtaining broadband inversion profiles and distortion-free lineshapes for spin-1/2, 1, and 3/2 nuclides. Similar pulses can be utilized during the spin-lock period of a CPMAS-type sequence, as possible routes for obtaining broadband CP under MAS conditions. Shown in Fig. 4A is the prototypical BRAIN-CPMAS sequence utilized in our simulations and experiments to test this: it involves a hard $\pi/2$ pulse on the $I = 1/2$ spins, followed by a spin lock of the transverse magnetization for a time t_p . A WURST pulse is simultaneously applied on

the S -spins (typical phase and amplitude profiles are shown in Fig. 4B). For the static BRAIN-CP case, any S -magnetization accumulated over the course of the spin lock will follow the S -spin’s adiabatic inversion pathway that an adiabatic pulse creates along the $S_z - S_x$ plane in the FM frame. Thus, CP-generated S -magnetizations will end up aligned along the z -axis at the completion of the contact time. A 90° “read” pulse is required to convert the S_z magnetization into detectable transverse coherences. Under conditions of MAS this relatively simple process is influenced by additional phenomena, owing in part to the various effects discussed in Section 2. In the following subsections, we briefly describe the features of these BRAIN-CPMAS effects, for each of the spin-1/2, spin-1, and half-integer quadrupolar spin ($\geq 3/2$) cases.

3.1. The frequency-swept CPMAS Hamiltonian for an I - $S(1/2)$ spin pair

For clarifying the behavior of the BRAIN-CPMAS mechanism, we consider an isolated $I(1/2)$ - $S(1/2)$ dipolar pair, where the I (^1H) spin is locked on resonance (i.e., $\Omega_I = 0$), and the S -spin has a $\delta_{CSA} = 0$. For the BRAIN-CP pulse sequence shown in Fig. 4A, the Hamiltonian of an isolated $I(1/2)$ - $S(1/2)$ dipolar pair under MAS is first considered in the doubly-rotating frame [19,20,90] and then further transformed into the

S-spin's FM frame. This results in

$$H_{I-S}^{FM}(t) = -\omega_{II}I_x - \Omega_S'(t)S_z - \omega_{IS}S_x + 2b(t)I_zS_z, \quad (32)$$

where $\omega_{II}(=\gamma_I B_{II})$ is the RF field strength applied to I , $\Omega_S'(t) = \Omega_S - \omega_p(t)$ is the offset of the S -spin in its FM frame, including the instantaneous offset frequency $\omega_p(t)$ coming from the sweep, ω_{IS} is a square-shaped RF chirp pulse applied on the S -spin (i.e., we assume $A(t) = 1$ for simplicity), and $2b(t)I_zS_z$ is a heteronuclear dipolar coupling interaction that under MAS is modulated as [18].

$$b(t) = \sum_{k=-2, k \neq 0}^2 b_k e^{ik\omega_r t}, \quad (33)$$

where the $\{b_k\}$ coefficients have the usual Euler angle dependencies in the I - S dipolar tensor defined in the principal axes system of the rotor frame [18].

Eq. (32) possesses dual time modulations originating from the adiabatic pulse and the ν_r -driven MAS modulations of the dipolar coupling interaction. For a fast spinning and a slow adiabatic sweep ($\nu_r \geq 30$ kHz, $t_p \geq 5$ ms), an average Hamiltonian considered over the time scale of a rotor period can be approximated by assuming a quasi-static offset for each rotor period. Then, by approximating the $\omega_p(t_0)$ in $\Omega_S'(t)$ as constant for time intervals $t = t_0$ to $t = t_0 + 2\pi/\omega_r$, a rotational transformation into a doubly-tilted frame where all RF fields are parallel to z' axes [18,90], leads to

$$H_T(t) = -\omega_{II}I_z - \omega_{eS}(t_0)S_z + 2 \sin \theta_S(t_0)b(t)I_xS_x, \quad (34)$$

where only the terms relevant for describing the CP phenomenon are kept [68]. In Eq. (34), the effective RF field strength along the tilted z' -axis of S is given by

$$\omega_{eS}(t_0) = \sqrt{\omega_{IS}^2 + [\Omega_S'(t_0)]^2} = \omega_{IS} \left[1 + \frac{1}{\omega_{IS}^2} \left(\Omega_S + \frac{\Delta\omega}{2} - \frac{\Delta\omega}{t_p} t_0 \right)^2 \right]^{1/2}, \quad (35)$$

and the $\sin(\theta_S[t_0])$ term, with a tilt angle $\theta_S(t_0)$ that relates the tilted z' -axis to the original z -axes in the FM frame, is given by

$$\sin(\theta_S[t_0]) = \omega_{IS}/\omega_{eS}(t_0) = \left[1 + \frac{1}{\omega_{IS}^2} \left(\Omega_S + \frac{\Delta\omega}{2} - \frac{\Delta\omega}{t_p} t_0 \right)^2 \right]^{-1/2}. \quad (36)$$

Utilizing a single-transition operator notation, Eq. (34) can be rewritten as [18,91]:

$$H_T(t) = -\omega_{\Delta}(t_0)I_z^{2,3} - \omega_{\Sigma}(t_0)I_z^{1,4} + \frac{\omega_{IS}b(t)}{\omega_{eS}(t_0)}(I_x^{2,3} + I_x^{1,4}) \quad (37)$$

where $\omega_{\Delta}(t_0) = \omega_{II} - \omega_{eS}(t_0)$, $\omega_{\Sigma}(t_0) = \omega_{II} + \omega_{eS}(t_0)$, and $I_{\xi}^{s,t}$ ($\xi = x, y, \text{ or } z; s, t = 2, 3 \text{ or } 1, 4$) are single-transition operators defined by:

$$\begin{aligned} I_z^{2,3} &= \frac{I_z - S_z}{2}, I_z^{1,4} = \frac{I_z + S_z}{2}; \\ I_x^{2,3} &= \frac{I_+S_- + I_-S_+}{2}, I_x^{1,4} = \frac{I_+S_+ + I_-S_-}{2}; \\ I_y^{2,3} &= \frac{I_+S_- - I_-S_+}{2i}, I_y^{1,4} = \frac{I_+S_+ - I_-S_-}{2i} \end{aligned} \quad (38)$$

acting in either the $\{|2\rangle, |3\rangle\}$ or $\{|1\rangle, |4\rangle\}$ subspaces. Because the single transition operators commute with each other, $H_T(t)$ in Eq. (37) can be written as a direct sum of two separate pseudo- 2×2 matrices

$$H_T^{2,3}(t) = -\omega_{\Delta}(t_0)I_z^{2,3} + \frac{\omega_{IS}b(t)}{\omega_{eS}(t_0)}I_x^{2,3} \quad (39)$$

and

$$H_T^{1,4}(t) = -\omega_{\Sigma}(t_0)I_z^{1,4} + \frac{\omega_{IS}b(t)}{\omega_{eS}(t_0)}I_x^{1,4}. \quad (40)$$

These equations determine the zero-quantum (ZQ) and double-quantum (DQ) CP processes, respectively.

By applying an $U_p = \exp(ik\omega_r t_z^{s,t})$ transformation onto the $H_T^{s,t}$ Hamiltonians in Eqs. (39) and (40) [18].

$$\tilde{H}_T^{s,t}(t) = U_p H_T^{s,t}(t) U_p^{-1} - i U_p \frac{d}{dt} U_p^{-1}, \quad (41)$$

the zeroth-order average Hamiltonians over a rotor period can be calculated by taking an integral over a time period of $t_r = \frac{2\pi}{\omega_r}$:

$$\langle \tilde{H}_T^{s,t} \rangle_{av} = \frac{1}{t_r} \int_0^{t_r} \tilde{H}_T^{s,t}(t) dt, \quad (42)$$

leading to

$$\langle \tilde{H}_T^{s,t} \rangle_{av} = [-\omega_{II} - k\omega_r + m\omega_{eS}(t)]I_z^{s,t} + \frac{b_k\omega_{IS}}{2\omega_{eS}(t)}I_x^{s,t}. \quad (43)$$

Here, m is $+1$ for the ZQ process and -1 for the DQ CP process, $k = \pm 1$ and ± 2 , $I_x^{s,t} = I_x^{s,t} + iI_y^{s,t}$, and t_0 has been generalized for simplicity to any time $0 \leq t \leq t_p$ within the sweep.

3.2. The frequency-swept CPMAS Hamiltonian for an $I - S(1)$ spin pair

These considerations can be extended to describe the Hamiltonian for an $I \rightarrow S(1)$ CP dynamics for a system subject to a frequency swept pulse on the S -spins under fast MAS. The CP Hamiltonian paralleling the spin-1/2 Eq. (32) counterpart is then:

$$\tilde{H}_T^{EM}(t) = -\omega_{II}I_x - \Omega_S'(t)S_z - \omega_{IS}S_x \cos \left(\int_0^t 3\chi_Q \omega_Q(t') dt' \right) + 2b(t)I_zS_z. \quad (44)$$

Here, the definitions of the terms and conditions are the same as previously, except for the addition of a quadrupole-modulated RF Hamiltonian. Applying a transformation into a doubly-tilted frame where all RF fields lie parallel to the z' axes [18,90] and considering only the relevant terms that drive the CP process, the isolated spin-pair CP Hamiltonian becomes [69].

$$\tilde{H}_T'(t) = -\omega_{II}I_z - \omega_{eS}(t)S_z + 2 \sin \theta_I \sin \theta_S(t)b(t)I_xS_x. \quad (45)$$

The effective resonance frequencies along these tilted z' -axes are ω_{II} and

$$\omega_{eS}(t) \approx \sqrt{\left\{ \Omega_S'(t) \right\}^2 + \omega_{IS}^2 \cos^2 \left(\int_0^t 3C_Q \omega_Q(t') dt' \right)}; \quad (46)$$

while the tilt angles θ_I and $\theta_S(t)$ that relate the z' -axes to the z -axes in the FM frame are given by $\sin(\theta_I) = 1$ and

$$\cos(\theta_S[t]) = \left(\Omega_S + \frac{\Delta\omega}{2} - \frac{\Delta\omega}{t_p} t \right) / \omega_{eS}(t), \quad (47)$$

$$\begin{aligned} \sin(\theta_S[t]) &= \omega_{IS} \cos \left(\int_0^t 3C_Q \omega_Q(t') dt' \right) / \omega_{eS}(t) \\ &= \frac{\omega_{IS} \sum_{k=-\infty}^{\infty} A_k^Q \exp(ik\omega_r t)}{\omega_{eS}(t)}, \end{aligned} \quad (48)$$

where the last relation uses the fact that $\sin(\theta_S[t])$ involves a Bessel integral that can be expanded as an infinite Fourier series. With these definitions and assumptions, Eq. (45) is rewritten as [17,18,92]:

$$\begin{aligned} \tilde{H}_T'(t) = & -\omega_{1I}I_z - \omega_{eS}(t)S_z \\ & + \frac{2\omega_{1S}\sum_{k=-\infty}^{\infty} A_k^Q \exp(ik\omega_r t) \sum_{k=-2}^2 b_k \exp(ik\omega_r t)}{\omega_{eS}(t)} I_x S_x. \end{aligned} \quad (49)$$

The product of the $\omega_r t$ -dependent Fourier expansions arising from the modulation of the quadrupolar and dipolar terms in Eq. (49), can be separated into time-independent and time-dependent terms:

$$\begin{aligned} \tilde{H}_T'(t) = & -\omega_{1I}I_z - \omega_{eS}(t)S_z \\ & + \frac{2\omega_{1S}[\Lambda_0 + \Lambda_{\pm 1}e^{\pm i\omega_r t} + \Lambda_{\pm 2}e^{\pm 2i\omega_r t} + \text{higher-order terms}]}{\omega_{eS}(t)} I_x S_x, \end{aligned} \quad (50)$$

where an explicit derivation of these $\Lambda_k(k=0, \pm 1, \text{ and } \pm 2)$ terms is summarized in our previous publication [70].

Utilizing the single-transition operator formalism and by separating the ZQ and DQ coherences, Eq. (50) can be separated and rewritten as:

$$\tilde{H}_T^{ZQ}(t) = -\omega_{\Delta}(t)I_z^{ZQ} + \frac{\omega_{1S}[\Lambda_0 + \Lambda_{\pm 1}e^{\pm i\omega_r t} + \Lambda_{\pm 2}e^{\pm 2i\omega_r t} + \dots]}{\omega_{eS}(t)} I_x^{ZQ} \quad (51)$$

and

$$\tilde{H}_T^{DQ}(t) = -\omega_{\Sigma}(t)I_z^{DQ} + \frac{\omega_{1S}[\Lambda_0 + \Lambda_{\pm 1}e^{\pm i\omega_r t} + \Lambda_{\pm 2}e^{\pm 2i\omega_r t} + \dots]}{\omega_{eS}(t)} I_x^{DQ}, \quad (52)$$

where, $\omega_{\Delta}(t)$, $\omega_{\Sigma}(t)$, and I_x^{ZQ} and I_x^{DQ} are as defined in Eqs. (37) and (38). Notice that Eqs. (51) and (52) again possess dual time dependencies, due to the frequency-swept pulses and the MAS-driven modulation. The same reasoning as described above can be used to remove the dual time dependencies under conditions of a slow-frequency swept pulse and fast MAS. If $\omega_{eS}(t)$ is approximated as quasi-constant for time intervals $t_0 \leq t \leq t_0 + \frac{2\pi}{\omega_r}$, the effective resonance frequency on the S channel can be averaged for each rotor period as

$$\omega_{eS}(t_0) \approx \sqrt{\left\{ \Omega_S + \frac{\Delta\omega}{2} - \frac{\Delta\omega}{T_p} t_0 \right\}^2 + \omega_{1S}^2}. \quad (53)$$

At a similar level of approximation, an evaluation of the argument in the

$\cos^2\left(\int_0^{\frac{2\pi}{\omega_r}} 3C_Q\omega_Q(t)dt\right)$ term contributing to $\omega_{eS}(t_0)$ over a rotor period

leads to a null average integral, and therefore

$\cos^2\left(\int_0^{\frac{2\pi}{\omega_r}} 3C_Q\omega_Q(t)dt\right) = 1$ is satisfied. With these assumptions, average

Hamiltonians over a rotor period $\langle H_T^{\zeta} \rangle_{av} = \frac{1}{\tau} \int_0^{\tau} H_T^{\zeta}(t)dt$, $\zeta = \text{ZQ or DQ}$, can be obtained from Eqs. (51) and (52) via the transformation $U_p H_T^{\zeta} U_p^{-1} - iU_p \frac{d}{dt} U_p^{-1}$, where $U_p = \exp(ik\omega_r t I_z^{\zeta})$ and $\zeta = \text{DQ or ZQ}$ refers to the zero- or double-quantum sub-spaces. This evaluation produces

$$\langle H_T^{\zeta} \rangle_{av} = [-(\omega_{1I} - k\omega_r) + m\omega_{eS}(t)] I_z^{\zeta} + \frac{\omega_{1S}\Lambda_k}{2\omega_{eS}(t)} I_x^{\zeta}, \quad (54)$$

where $k = \pm 1$ and ± 2 , $I_{\pm}^{\zeta} = I_x^{\zeta} + iI_y^{\zeta}$ ($\zeta = \text{ZQ or DQ}$), m is $+1$ for the ZQ-CP process and -1 for the DQ-CP process. In the above equations, t_0 has been generalized for simplicity to a generic time t .

While the $k = \pm 1, \pm 2$ terms in Eq. (54) are the same as for CPMAS

experiments involving spin-1/2 nuclides, the static-like polarization transfer process involving the Λ_0 term is peculiar to CPMAS of quadrupoles, and arises due to the interference between the periodic quadrupole-driven modulation of the RF, and the identically periodic MAS-driven modulation of the dipolar coupling. This recoupling effect can be separated from Eq. (51); for a dipole-coupled $I = 1/2 - S = 1$ spin pair it is given by

$$\langle H_T^{ZQ} \rangle_{av} = [-\omega_{1I} + \omega_{eS}(t)] I_z^{ZQ} + \frac{\omega_{1S}\Lambda_0}{\omega_{eS}(t)} I_x^{ZQ}. \quad (55)$$

When $\omega_{1I} = \omega_{eS}(t)$, this CP mode will transfer I -magnetization to the S -spin. Notice that, as is the case for static solids, only a ZQ HH match is possible; a DQ-HH process is not allowed because there is not a condition nulling the coefficient of I_x^{DQ} in Eq. (52), $\omega_{\Sigma}(t)$, for any combination of ω_{1I} and $\omega_{eS}(t)$. The relevance and magnitude of Λ_0 term can be evaluated by considering an example. For instance, for a crystallite orientation ($\beta = 45^\circ, \gamma = 0^\circ$) of a dipolar coupled $^1\text{H}-^2\text{H}$ pair collinear with the largest component of an axially-symmetric EFG tensor, possessing a $^1\text{H}-^2\text{H}$ dipolar coupling of 4 kHz and a $C_Q = 168$ kHz, the magnitude of the quadrupole-driven RF-dipolar recoupled term Λ_0 is about 680 Hz [69]. The magnitude of this coefficient is significant, and can generate a static-like, $k = 0$, ZQ0 CP mode even under very fast MAS.

3.3. The frequency-swept CPMAS Hamiltonian for an $I-S(\geq 3/2)$ spin pair: transfer dynamics to the central transition of a half-integer quadrupolar nuclide

Employing Eq. (31) as a starting point, the Hamiltonian necessary for describing $I(1/2) \rightarrow S(\geq 3/2)$ BRAIN-CPMAS requires the inclusion of an RF term for the I -spin as well as an I - S dipolar coupling term. Again, any potential homonuclear I - I and S - S dipolar coupling interactions and I - and S -spin CSAs are ignored for simplicity. The $I \rightarrow S(\geq 3/2)$ CP process is further separated into separate $I \rightarrow S(\text{CT})$ and $I \rightarrow S(\text{TQ})$ CP processes, described by the S_x^{2-3} and S_x^{2-3} and S_z^{1-4} and S_x^{1-4} operators, respectively; for simplicity, only the $I \rightarrow S(\text{CT})$ transfer is here taken into consideration. This simplification is justified because, although these two dynamic processes are not decoupled from one another, the RF Hamiltonian that contains a S_x^{2-3} operator can effectively spin-lock the CT coherence when a small ν_{1S} value is employed (see Fig. 3). As demonstrated by A. Vega [75], when the adiabaticity parameter is small ($\alpha = \frac{\nu_{1S}^2}{\chi_Q \nu_r} \ll 1$), both the TQC term and the oscillating terms arising in the quadrupolar interaction frame that connect the CTC to other coherences can be safely ignored. Then, considering the Hamiltonians in the doubly rotating frame, and proceeding as before with a series of transformations taking us first into a FM frame and then into S 's quadrupolar interaction frame, the Hamiltonian for the $I \rightarrow S(\text{CT}; S = 3/2)$ CP polarization transfer in the relevant S_x^{2-3} ($\xi = x \text{ or } z$) subspace is

$$H_{I-S}^{CP}(t) = -\omega_{1I}I_x + \left\{ \Omega_S'(t) + \Omega_{QS}^{2-3}(t) + 2b(t)I_z \right\} S_z^{2-3} + 2\omega_{1S}S_x^{2-3}. \quad (56)$$

This expression can be readily extended to higher half-integer quadrupolar nuclei ($S = 5/2, 7/2, \text{ or } 9/2$), by defining $S_z = S_z^{c-t}$ and $S_x = \left(S + \frac{1}{2} \right) S_x^{c-t}$, where $c-t$ stands for 3-4, 4-5 and 5-6 for $S = 5/2, 7/2$ and $9/2$, respectively. Notice that unlike the spin-1 case, the RF term in Eq. (56) is free from the modulation of quadrupolar interaction because the CTC of a half-integer S -spin is not influenced by the first-order quadrupolar interaction.

Using these fictitious spin-1/2 operators, Eq. (56) becomes

$$H_{I-S}^{CP}(t) = -\omega_{1I}I_x + \left\{ \Omega_S'(t) + \Omega_{QS}^{c-t}(t) \right\} S_z + \omega_{1S}S_x + 2b(t)I_z S_z. \quad (57)$$

Except for the presence of an additional $\Omega_{QS}^{c-t}(t)$ term representing the

second-order quadrupolar interaction offset the central transition, Eq. (57) is identical to the previous equation for the $I \rightarrow S(1/2)$ BRAIN-CPMAS, Eq. (32). The expression of $\Omega_{Q,S}^{c-t}(t)$ for an arbitrary half-integer quadrupolar spin S is:

$$\Omega_{Q,S}^{c-t}(t) = \frac{3}{\omega_0} \chi_Q^2 [4S(S+1) - 3] \times \sum_{m=-4}^4 \omega_Q^m(\alpha, \beta) \exp[im(\gamma + \omega_r t)], \quad (58)$$

where explicit expressions for $\omega_Q^m(\alpha, \beta)$ are summarized in our previous publication [70].

Since Eq. (57) is identical in form to the simplest $I \rightarrow S(1/2)$ CP case, the equations that define it are identical to those outlined in the procedure for the $I \rightarrow S(1/2)$ CP case. Thus, average Hamiltonians that predict the ZQ- and DQ-CP processes over a rotor period for the $I \rightarrow S(CT; S \geq 3/2)$ polarization transfer involved in the BRAIN-CPMAS mixing are written as [68,70].

$$\langle H_T^c \rangle_{av} = [- (\omega_{11} - k\omega_r) + m \omega_{es}(t)] I_z^c + \frac{\omega_{1S} b_k}{2 \omega_{es}(t)} I_{\pm}^c, \quad (59)$$

where

$$\omega_{es}(t) = \sqrt{\left\{ \Omega_S + \Omega_{Q,S}^{c-t}(t) + \frac{\Delta\omega}{2} - \frac{\Delta\omega}{t_p} I \right\}^2 + \omega_{1S}^2}, \quad (60)$$

with $k = \pm 1$ and ± 2 , $I_{\pm}^c = I_x^c \pm iI_y^c$ ($\zeta = \text{ZQ}$ or DQ), and m is $+1$ for the ZQ-CP process or -1 for the DQ-CP process.

3.4. Fulfilling the HH matching conditions over the course of a swept pulse

Having derived the relevant Hamiltonians, the time-dependent ZQ and DQ HH matching conditions for the swept CPMAS experiment can be discussed. These can be determined by inspecting the coefficients of the longitudinal z -terms in Eqs. (43), (54), (55) and (59), for $S = 1/2$, $S = 1$ and $S \geq 3/2$ (CT) spins, respectively. A common property of these equations is the presence of a ZQ_k HH transfer mode, that is satisfied when the condition $\nu_{es}(t) - \nu_{11} + k\nu_r = 0$ ($k = -1$ or -2) is fulfilled. Likewise, a DQ_k HH transfer occurs at a time t when the condition $\nu_{es}(t) + \nu_{11} - k\nu_r = 0$ ($k = 1$ or 2) is met. These CP conditions are satisfied whenever the time-dependent conditions that make the I_z^{ZQ} or I_z^{DQ} coefficients zero –which are conditions that enable the I -spin to transfer its polarization. Because of the time-dependent nature of the $\omega_p(t)$ term in $\omega_{es}(t)$, these matching conditions will be satisfied only for a few instants over the course of the contact time. This is illustrated in Fig. 5A and B for $I(1/2)$ - $S(1/2)$ and $I(1/2)$ - $S(1)$ cases, respectively, which show ZQ_k and DQ_k HH matching curves calculated for a variety of $\Omega_S/2\pi$ offset frequencies under fast MAS rates. Black dots indicate the times at which the various DQ_k and ZQ_k matching are satisfied and CP transfer occurs.

Notice from Fig. 5A that as a result of the $\omega_p(t)$ dependence of $\omega_{es}(t)$, both DQ- and ZQ-CP matching conditions can be met twice, at two different times t_1 and t_2 , throughout the course of a swept pulse. Depending on Ω_S , these time points may or may not fall within the $0 \leq t \leq t_p$ period, and hence, may or may not be relevant to the CP process. If $\Omega_S/2\pi = 0$, these t_1 and t_2 points are mirror images of each other across the center point of the symmetric frequency sweep. If an off-resonance frequency contribution is considered, these t_1 and t_2 time points shift uniformly for the DQ_1 conditions to earlier times when $\Omega_S < 0$ and to later times when $\Omega_S > 0$. Conversely, if the frequency offset is in the range of $|\nu_r|/2 < |\Omega_S|/2\pi < |\nu_r|$, only a single contact time is found in the time period $0 \leq t \leq t_p$, with the other appearing at either $t > t_p$ ($\Omega_S > 0$) or at $t < 0$ ($\Omega_S < 0$). For offset-frequencies in the $|\Omega_S|/2\pi > |\nu_r|$ range, both CP-contact time points of DQ_1 disappear from the physically meaningful $0 \leq t \leq t_p$ window; in their absence, other modes such as DQ_2 , ZQ_{-1} , and ZQ_{-2} may become more significant. Moreover, if parameters are optimized to produce an efficient DQ_1 mode in the central $\Omega_S \approx$

0 spectral region, other modes such as DQ_2 , ZQ_{-1} , and ZQ_{-2} will not contribute to the CP signal transfer within the physically-meaningful $0 \leq t \leq t_p$ mixing interval. Similar considerations can be derived for the remaining DQ_2 , $\text{ZQ}_{\pm 1}$ and $\text{ZQ}_{\pm 2}$ transfer modes. One interesting property is that if CP transfer times are met for $\Omega_S/2\pi$ at certain values of t_i , those for $-\Omega_S/2\pi$ will be met at $t_p - t_i$ (Fig. 5A).

Fig. 5B presents simulated results of ^1H - ^2H BRAIN-CPMAS dynamics by incorporating several different offset frequencies $\Omega_S/2\pi$ (0, ± 32 , and ± 60 kHz), and assuming null and non-null quadrupole couplings ($\nu_r = 60$ kHz). Also illustrated are the fulfillment of DQ_k ($k = 1, 2$) and $\text{ZQ}_{\pm k}$ ($k = 1$ or 2) conditions, as well as the propagation of the S -spin spin-locked (S_z) and transverse (S_x) magnetizations, arising from a situation where these are null at the beginning of the spin-lock when only I_x polarization exists. Apart from the scaling effects of the 2 and $\sqrt{2}$ coefficients present in the $S_z^{1/2}$ and $S_x^{1/2}$ operators, respectively, these predictions are similar to those made for the $S = 1/2$ case when $C_Q = 0$. The time points at which CP transfers occur associated with the ZQ and DQ conditions are clearly connected with $I \rightarrow S$ transfers of spin-locked polarization, and time points during the swept pulse period measured at any arbitrary offset frequencies satisfy the same mirror image rules as found in the I - $S(1/2)$ case. A major difference worth noting between the present $S = 1$ case and the earlier spin- $1/2$ analysis, concerns the appearance of new ZQ_0 -derived HH transfers. This is as predicted by Eq. (55): a static-like ZQ_0 condition arises for a I - $S(1)$ spin pair even under a ultrafast spinning rate because of the occurrence of quadrupolar-driven RF-dipolar recoupling under MAS. It is also noteworthy that the introduction of $C_Q \neq 0$ breaks the symmetry of the aforementioned transfers of the two time points from each CP mode (middle row in Fig. 5B). For instance, while the polarization transfers at two symmetric time points that satisfy the DQ_1 condition are clearly visible when $C_Q = 0$ for the on-resonance case, an attenuation at the later time point is noticeable in the presence of a larger magnitude of C_Q ($= 168$ kHz). This may help to create non-zero S_z polarization at the conclusion of the swept pulse.

As in the previous two cases, time-dependent ZQ- and DQ-HH matching conditions can be found from the $I \rightarrow S(CT; S \geq 3/2)$ dynamics over the entire contact time during the course of the frequency swept pulse. A $\text{ZQ}_{\pm k}$ ($k = 1$ or 2) HH matching condition is satisfied when the effective frequency, $\nu_{es}(t)$ – which depends on ν_{1S} , Ω_S , $\omega_p(t)$, and the orientation-dependent second-order quadrupolar frequency $\Omega_{Q,S}^{c-t}(t)$ – instantaneously satisfies $\nu_{11} - \nu_{es}(t) = \pm k\nu_r$. In a similar manner, a DQ_k ($k = 1$ or 2) HH matching condition is met when $\nu_{es}(t)$ satisfies $\nu_{11} + \nu_{es}(t) = k\nu_r$. A difference, however, now stems from the presence of the second-order quadrupolar terms in the effective offset frequency $\nu_{es}(t)$, that is instrumental in defining these HH matching conditions (Eqs. [59] and [60]). Moreover, the non-vanishing, MAS-averaged, second-order quadrupolar effects [89] impose powder angle dependencies of the EFG tensor on the ZQ- and DQ-matching conditions. Fig. 6 shows numerical simulations of $I \rightarrow S(CT; S = 3/2)$ BRAIN-CPMAS profiles derived from these considerations. These simulations incorporate parameters for an isolated I - S pair that are taken from ^1H - ^{11}B BRAIN-CPMAS experiments on sodium tetraborate decahydrate (*vide infra*), assuming moderately fast $\nu_r = 25$ kHz. Fig. 6A shows the ZQ- and DQ-HH conditions revealed as a function of the I -spin RF strength (ν_{11}) for a fixed ν_{1S} . Because of the orientation-dependent quadrupolar frequency dispersion in $\nu_{es}(t)$, numerous local maxima and minima showing positive and negative signal enhancements of the CTC arise. Still, the ZQ_{-1} , ZQ_{-2} , DQ_1 , and DQ_2 conditions are all clearly visible in this RF field profile, with the signal enhancements from ZQ- and DQ-HH matching conditions possessing the expected opposite signs. Illustrated in Fig. 6B and E are the time-dependent transfer dynamics of I_x , S_x , and S_z for the (B) DQ_1 , (C) DQ_2 , (D) ZQ_{-1} , and (E) ZQ_{-2} conditions found in Fig. 6A. In these cases, the spin-locked (S_z) and transverse (S_x) states are null at the beginning of the swept pulse, with all polarization at I_x . As the offset of the S -spin RF changes over the duration of the swept pulse, the magnetization of the

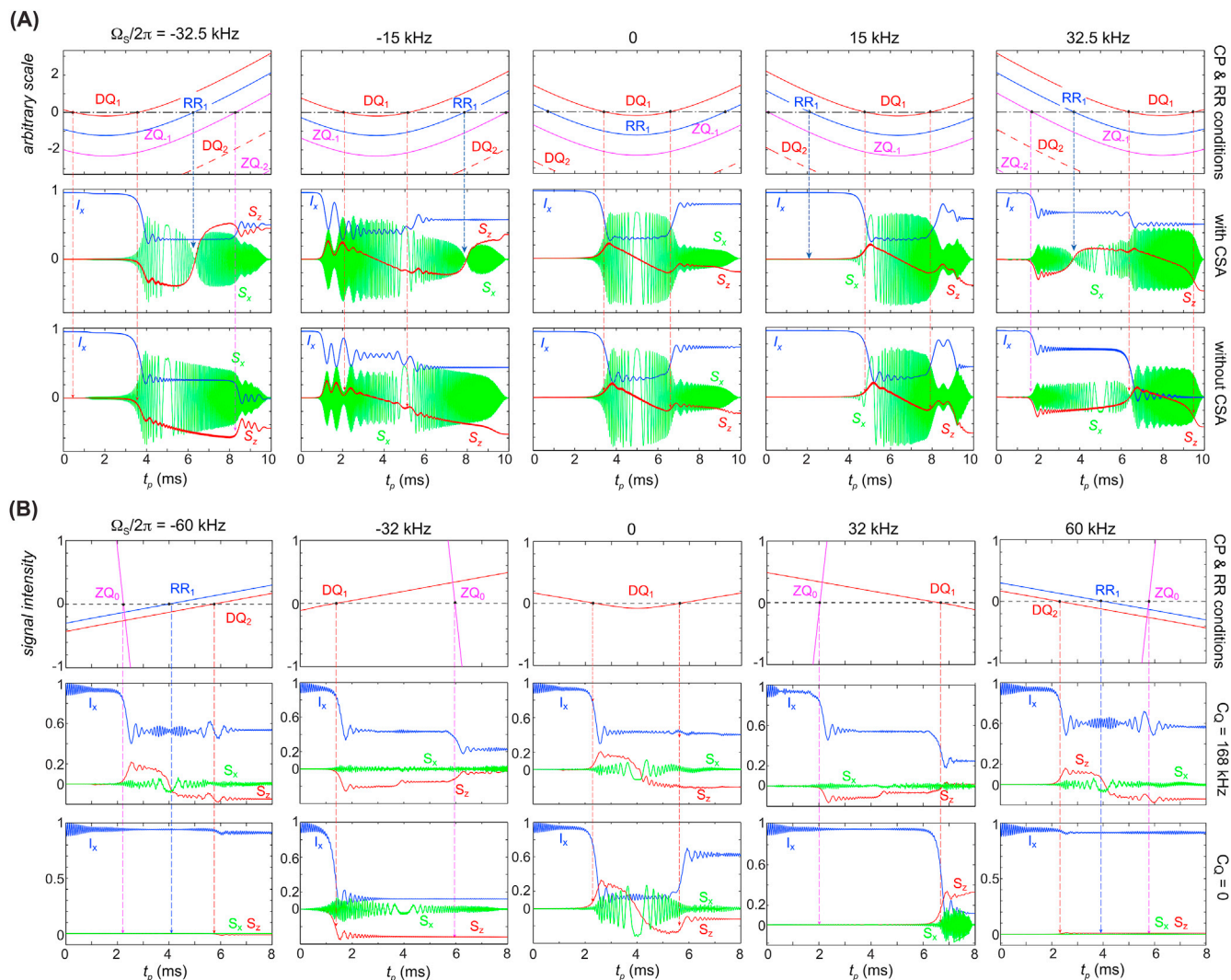


Fig. 5. CP transfer and RR inversion conditions calculated for a swept BRAIN-CPMAS for a spin pair of (A) $I(1/2)$ - $S(1/2)$ ($\nu_r = 65$ kHz; $\Delta\nu = 110$ kHz; $t_p = 10$ ms; $\nu_{1S} = 45$ kHz; $\nu_{1I} = 17$ kHz) and (B) $I(1/2)$ - $I(1/2)$ ($\nu_r = \Delta\nu = 60$ kHz; $t_p = 8$ ms; $\nu_{1S} = 5$ kHz; $\nu_{1I} = 47$ kHz). Shown in the top rows in (A) and (B) are various types of DQ (red line) and ZQ (magenta line) matching conditions shown at the specified Ω_S offsets in terms of the time points (zero crossing conditions) at which CP signal transfers occur. Also shown are curves showing the positions that satisfy the RR condition $\nu_{eS}(t) = \nu_r$, occurring during the CP mixing time in the presence of an S -spin's (A) CSA ($\delta_{CSA} = 18$ kHz, $\eta = 0$) and (B) $H_{QS}^{(1)}$ ($C_Q = 168$ kHz, $\eta = 0$; $\delta_{CSA} = 0.92$ kHz). Time propagations of an initial I_x state (blue) and of the CP-enhanced S_x (green) and S_z (red) polarizations, recorded with (middle row) and without (bottom row) the inclusion of CSA (A) and C_Q (B) effects. Notice the sign inversion of the CP-enhanced S_z -components occurring at the time points at which a RR condition is satisfied – but only when CSA and/or C_Q is included. (For interpretation of the references to color in this figure legend, the reader is referred to the Web version of this article.)

spin-locked state grows gradually, via HH transfers associated with the DQ_k and $ZQ_{\pm k}$ ($k = 0, 1$ or 2) conditions.

While similar mechanisms are active in BRAIN-CPMAS in the I - S (CT; $S \geq 3/2$) case as in the I - $S(1/2)$ and I - $S(1)$ cases, there are a number of peculiarities in the dynamics, as shown in Fig. 7. These include: (1) RF scaling effects coming from the coefficient 2 in front of the $S_x^{1/2}$ operator; (2) the absence of sharp S_z or S_x buildup points associated with the fulfillment of $\pm\nu_{eS}(t) - \nu_{eI} \mp k\nu_r = 0$ ($k = 1$ or 2) conditions throughout the powdered sample; (3) the fact that polarization accrued by the S -spin during the BRAIN-CP process stays mainly as a longitudinal magnetization S_z without developing any significant transverse components, S_x and S_y (only S_x is shown in the figure); and (4) the fact that the CP-enhanced S_z magnetization does not oscillate back to I_z (at least to some extent) during the CP mixing period, even though a single I - S pair is being considered. The last three of these features can be attributed to the presence of a distribution of second-order quadrupolar anisotropic frequencies, $\Omega_{QS}^{(2)}(t)$, in $\nu_{eS}(t)$. Because of these anisotropic

shifts, the $\pm\nu_{eS}(t) - \nu_{eI} \mp k\nu_r = 0$ conditions are met at different times over the course of the swept pulse for different crystal orientations, resulting in a spread of the HH transfer processes throughout the 0 - t_p time period. Consequently, one does not observe any specific time points that are explicitly associated with ZQ or DQ conditions. This “spreading effect” associated with $\Omega_{QS}^{(2)}$ also “washes out” the oscillating features of S_z magnetization transferred during the course of the BRAIN-CPMAS process, which therefore never returns back to I_z to any appreciable extent.

3.5. Onset of CSA- and quadrupolar-driven rotary resonance effects

An unusual aspect of BRAIN under MAS concerns the complex sign inversion behavior of the S -spin polarization that arises at the conclusion of the WURST pulse in BRAIN-CPMAS experiments due to rotary resonance (RR) effects. These complexities are illustrated in Fig. 5A and B, which show the time-dependent I_x (blue), S_x (green),

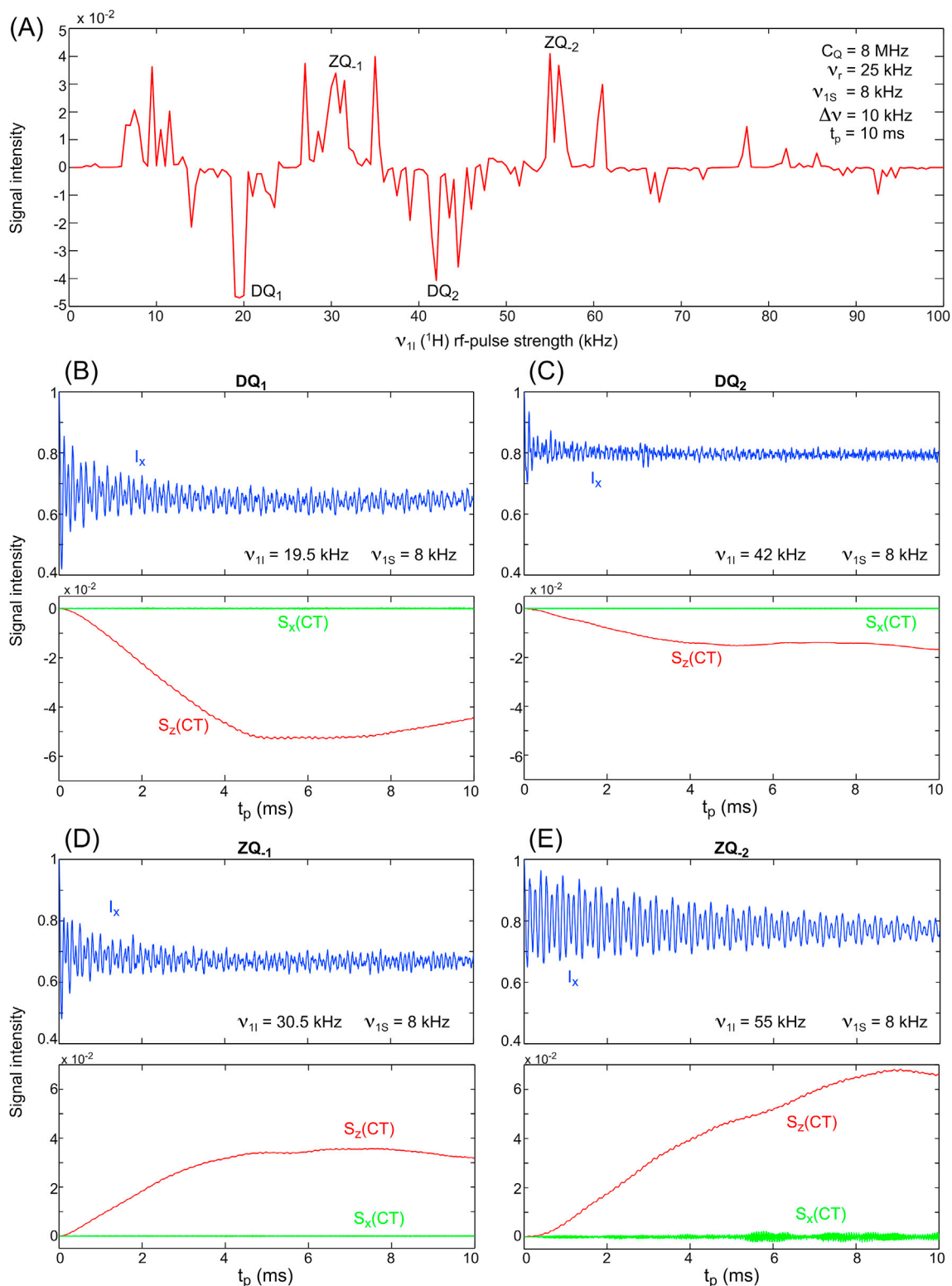


Fig. 6. CTC BRAIN-CPMAS transfer dynamics simulated for an isolated $I(1/2)$ - $S(3/2)$ spin pair with a dipolar coupling constant of 8 kHz. Simulations were carried out with $C_Q = 8$ MHz ($\eta_Q = 0$), $\nu_{OI} = 600$ MHz, $\nu_{OS} = 160.4$ MHz, and $\nu_{1S} = 8$ kHz, while varying ν_{1I} intensity. The WURST pulse parameters employed were $\Delta\nu = 10$ kHz and $t_p = 10$ ms. Time propagations of the initial I_x state (blue) and of the CP-enhanced S_x (green) and spin-locked S_z (red) polarizations of the S central transition are represented. Demonstrated are (A) the DQ_k and ZQ_k ($k = 1$ or 2) HH conditions found as a function of ν_{1I} for a fixed ν_{1S} (8 kHz), and the (B) DQ_1 , (C) DQ_2 , (D) ZQ_1 , and (E) ZQ_2 signal transfer dynamics. Simulations were carried out assuming on-resonance irradiation for I and a symmetric sweep about the S -spin CT second-order isotropic quadrupolar shift. (For interpretation of the references to color in this figure legend, the reader is referred to the Web version of this article.)

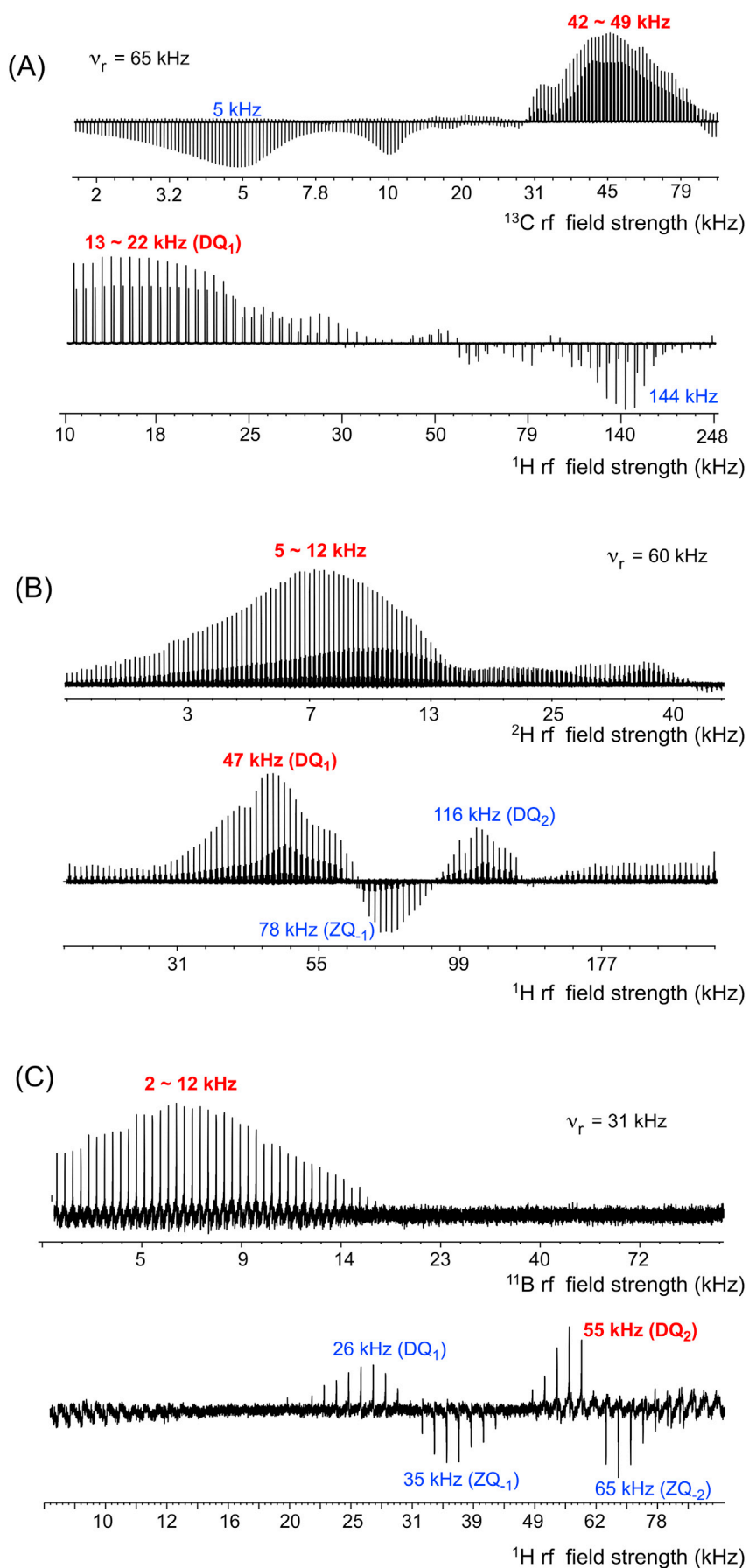


Fig. 7. Experimental (A) ^{13}C and ^1H (measured on $[1-^{13}\text{C}]$ Gly), (B) ^2H and ^1H (measured on glycine-2,2- d_2), and (C) ^{11}B and ^1H (measured on sodium tetraborate decahydrate) signal intensities obtained during the optimization of the BRAIN-CPMAS sequence by varying S (^{13}C , ^2H , or ^{11}B) and I (^1H) RF channel intensities. The optimal RF fields for experiments were set at: (A) $\nu_{1S}(^{13}\text{C}) = 45 \pm 4$ kHz and $\nu_{1I}(^1\text{H}) = 17 \pm 5$ kHz at $\nu_r = 65$ kHz; (B) $\nu_{1S}(^2\text{H}) = 8 \pm 4$ kHz and $\nu_{1I}(^1\text{H}) = 47 \pm 5$ kHz at $\nu_r = 60$ kHz; (C) $\nu_{1S}(^{11}\text{B}) = 5 \pm 3$ kHz and $\nu_{1I}(^1\text{H}) = 55 \pm 5$ kHz at $\nu_r = 31$ kHz. RF fields at the local maxima for other CP modes are also indicated, as derived from individual 90° pulse calibrations. The WURST pulse parameters employed were: (A) $\Delta\nu = 110$ kHz and $t_p = 10$ ms; (B) $\Delta\nu = 60$ kHz and $t_p = 8$ ms; (C) $\Delta\nu = 25$ kHz and $t_p = 4$ ms. The maximum experimental CP efficiency is obtained by DQ₁ mode for (A) and (B), and by DQ₂ mode for (C).

and S_z (red) transients involved in the CPMAS signal transfer dynamics in the presence of S -spin CSA (5A) and quadrupolar interaction (5B). Examination reveals that in the presence of even a small CSA or first-order quadrupolar interaction, a significant phenomenon begins to affect the swept-CP MAS experiment: this is the presence of $\pm S_z \rightarrow \mp S_z$ inversions, introducing in turn reversals in the phases of the S -peaks polarized over the course of this process. These changes in the peak phases are associated to MAS-driven RR effects [93,94]. With RR as a new mechanism capable of morphing a spin-locked magnetization parallel to the effective S -field into an “anti-spin-locked” state (and vice versa), one needs to consider how this factors into the signs of the S -spin polarizations that may have formed throughout the BRAIN-CPMAS process. Fig. 5 facilitates this, by illustrating the time points that satisfy the $\nu_{eS}(t) = \nu_r$ RR condition for a series of frequency offsets and parameters like those utilized above for calculating the swept CPMAS matching conditions. Highlighted in Fig. 5A and B are the RR time points that fall in the $0 \leq t \leq t_p$ range. Notice then that if a S -spin component has been generated by CP, it will be inverted by the CSA (5A) or quadrupolar interaction (5B) if this creation happened prior to a RR-driven S -spin event, but will remain spin-locked otherwise. Notice as well that for some offsets (e.g., the fourth column in Fig. 5A, $\Omega_S/2\pi = 15$ kHz), RR occurs before the HH transfer events, resulting in non-inverted signals after the CP event itself. Thus, curves calculated with $\Omega_S/2\pi = -15$ kHz (the second column in Fig. 5A) and with $\Omega_S/2\pi = 15$ kHz (the fourth column in Fig. 5A) possess S_z polarization with opposite signs at the completion of the CP mixing; by contrast, when the CSA interaction is not included, they have an identical signs. For other $\Omega_S/2\pi$ offsets (e.g., $\Omega_S/2\pi = \pm 32.5$ kHz in Fig. 5A) the RR inversion occurs after transfer events like DQ₁, resulting in an inversion of the CP signals. These features are clearly visible from the time-dependent S_x and S_z transients in Fig. 5A. Moreover, for the on-resonance case, two time points may satisfy the RR condition; since two inversions are the same as no inversion, there are no RR-driven effects on the final CP signal. These RR-driven effects can be generalized to arbitrary offset-frequencies. It then follows that, in general, the sign of S_z obtained upon sweeping around a particular Ω_S , will be 180° out-of-phase to that obtained from sweeping around $-\Omega_S$. Thus, in the presence of CSA, the S_z states calculated at $\pm\Omega_S$ are placed on the opposite hemispheres in the FM frame. This RR inversion effect takes place even when a CSA of small magnitude is present (even those small enough to have any manifestations of CSA effectively averaged from by MAS). Still, the effects of RR on the final state of the spin-locked magnetizations are remarkable but easily understandable.

These RR inversion phenomena can also be driven by modulations arising from the first-order quadrupolar interaction, yet they will not play an important role when sweeps are chosen such that $\Delta\nu \leq \nu_r$ and/or the $\Omega_S/2\pi$ offsets are small (Fig. 5B). However, they become noteworthy when the frequency offset becomes significant (e.g., $\Omega_S/2\pi = \pm 60$ kHz). Interestingly, the presence of the $\Omega_{QS}^{\zeta-t}(t)$ term in $\nu_{eS}(t)$ obscures this phenomenon somewhat; this is evident in the $I \rightarrow S(1/2)$ and $I \rightarrow S(S=1)$ cases [24,43]. Once again, second-order broadenings spread out this condition, implying that there will exist no singular time point over the course the adiabatic frequency sweep where the spin-locked S -spin polarization is suddenly inverted due to a RR condition.

3.6. Analytical time propagation of the spin ensemble throughout the BRAIN-CPMAS transfer

The rotationally-averaged Hamiltonians in Eqs. (43), (54) and (59) derived for $S = 1/2, 1$, and $\geq 3/2$ cases respectively, as well as the static-like Hamiltonian in Eq. (55) for $S = 1$, not only allow one to rationalize the behavior observed in numerical simulations, but also to analytically propagate the spin density matrix throughout the course of the frequency-swept pulse. Starting from a $\rho(t=0) = I_z = I_z^{DQ} - I_z^{ZQ}$ state, the spin polarization obtained from CP on the spin locked S -channel at a

time t_p , given by S_z in the FM frame, is described by Ref. [91].

$$S_z(t_p) = \text{trace}\{I_z^{DQ} U_{DQ}(t_p) I_z^{DQ} U_{DQ}^\dagger(t_p)\} - \text{trace}\{I_z^{ZQ} U_{ZQ}(t_p) I_z^{ZQ} U_{ZQ}^\dagger(t_p)\} \quad (61)$$

with

$$U_\zeta(t_p) = \exp\left(-i \int_0^{t_p} dt [\langle H_T^\zeta \rangle_{av}(t)]\right), \quad (62)$$

where ζ stands for a DQ- or ZQ-coherence. As the I_z^ζ and I_z^ζ terms in $\langle H_T^\zeta \rangle_{av}$ do not commute, Eq. (62) must, in principle, be evaluated numerically. However, if the adiabaticity of the WURST pulse employed is sufficiently high and the $d\theta_s(t)/dt \ll 1$ condition is satisfied, one can assume that perturbations in $\theta_s(t)$ are negligible, and hence, the angle between the S -spin magnetization and the effective field remain constant.² In such a case, an approximate average Hamiltonian over the whole mixing time, $\langle H_T^\zeta \rangle_{av}(t) = \frac{1}{t_p} \int_0^{t_p} \langle H_T^\zeta \rangle_{av}(t) dt$ may be obtained, by integrating I_z^ζ and I_z^ζ terms separately [44]. This treatment can be justified by considering the mechanism of polarization transfer for which the adiabaticity of the pulse employed fulfills $d\theta_s(t)/dt \ll 1$. Then, perturbations in $\theta_s(t)$ can be neglected and the angle between the spin magnetization and effective field assumed constant. In this case, the spins' evolution operator, Eq. (62), can be approximated as

$$\begin{aligned} U_\zeta(t_p) &\cong \exp\left(-it_p \overline{\langle H_T^\zeta \rangle_{av}(t)}\right) \\ &= \exp(i\theta^\zeta I_z^\zeta) \exp(i\theta^\zeta I_y^\zeta) \exp(-i\psi^\zeta I_z^\zeta) \exp(-i\theta^\zeta I_y^\zeta) \exp(-i\theta^\zeta I_z^\zeta). \end{aligned} \quad (63)$$

Eq. (63) represents a rotation in $\{\zeta\}$ subspace through an angle ψ^ζ about an axis whose orientation is described with a polar angle set $(\theta^\zeta, \phi^\zeta)$. Given these separate fictitious-spin- $1/2$ rotations, evaluation of Eq. (61) leads to

$$S_z(t_p) = \sin^2(\theta^{ZQ}) \sin^2\left(\frac{1}{2}\omega_{eff}^{ZQ} t_p\right) - \sin^2(\theta^{DQ}) \sin^2\left(\frac{1}{2}\omega_{eff}^{DQ} t_p\right), \quad (64)$$

where

$$\omega_{eff}^\zeta = \psi^\zeta / t_p = \sqrt{\Gamma^\zeta}, \quad (65)$$

$$\sin^2(\theta^\zeta) = \frac{C_k^2 \Pi_1^2}{\omega_{1S}^2 \Gamma^\zeta}, \quad (66)$$

$$\Gamma^\zeta = (\Pi_0 + \Pi_1 - m\omega_{1l})^2 + 2mk\omega_r(\Pi_0 + \Pi_1 - m\omega_{1l}) + k^2\omega_r^2 + \Lambda_k^2 \Pi_1^2 / \omega_{1S}^2, \quad (67)$$

$$\begin{aligned} \Pi_0 &= \frac{1}{2\Delta\omega} \left\{ \left(\Omega_S + \frac{\Delta\omega}{2} \right) \sqrt{\omega_{1S}^2 + \left(\Omega_S + \frac{\Delta\omega}{2} \right)^2} \right. \\ &\quad \left. - \left(\Omega_S - \frac{\Delta\omega}{2} \right) \sqrt{\omega_{1S}^2 + \left(\Omega_S - \frac{\Delta\omega}{2} \right)^2} \right\}, \end{aligned} \quad (68)$$

and

² For quadrupolar nuclei, $S \geq 1$, as can be inferred from the simulation data shown in Figs. 2 and 3, the choice of $\Delta\nu$ and ν_1 are very critical to satisfy this condition by avoiding the adiabatic level crossing effects. For $S \geq 3/2$ case, this condition is even more restrictive due to the presence of $\Omega_{QS}^{\zeta-t}(t)$ in the coefficient of I_z^ζ .

$$\Pi_1 = \frac{\omega_{1S}^2}{2\Delta\omega} \ln \left\{ \frac{(\Omega_S + \frac{\Delta\omega}{2}) + \sqrt{\omega_{1S}^2 + (\Omega_S + \frac{\Delta\omega}{2})^2}}{(\Omega_S - \frac{\Delta\omega}{2}) + \sqrt{\omega_{1S}^2 + (\Omega_S - \frac{\Delta\omega}{2})^2}} \right\}. \quad (69)$$

In Eq. (67), $\Lambda_k = b_k$ for the $S = 1/2$ and $\geq 3/2$ cases. Under these simplifications, the behavior for a quadrupolar nucleus will be identical to that derived earlier for $S = 1/2$ [68], except that the additional quadrupole-driven $k = 0$ ZQ-CP condition and the spin-dependent factors serve to scale the effects of the RF nutation rate.

4. Materials and methods

4.1. Numerical calculations

All simulations in this study were performed in the time-domain with full Hamiltonians for each I - S spin case, without any approximations other than the usual rotating frame transformation. These calculations were carried out by using in-house programs written in Matlab[®] (The Mathworks Inc). Evolutions of density matrices were evaluated numerically by considering piecewise time increments in steps of 2 μ s to take into account the variations of the amplitudes and phases of the RF pulses, as well as the MAS-driven rotational modulations of dipolar, CSA, and/or quadrupolar interactions. An isolated S -spin with anisotropic NMR interactions was considered for examining the inversions of longitudinal magnetizations, the lineshapes of spinning powders, as well as for considering the RR inversion effect. The actual CP process was examined by considering an isolated I - S ($S = 1/2, 1, \text{ or } \geq 3/2$) spin pair in the presence of a suitable MAS-modulated dipolar Hamiltonian. Powder averaging calculations of the S -spin's CSA and quadrupolar interactions as well as of the I - S dipolar coupling interaction were carried out by considering the 6044 and 1154 crystal orientations of the ZCW's Euler angle sets [95], assuming axially symmetric dipolar, CS, and EFG tensors for simplicity (in all cases, the relative tensor orientations are described by assuming that the principal components of largest magnitude from each tensor are coincident).

4.2. Experimental

BRAIN-CPMAS experiments were conducted on powdered samples of: 1) [$1\text{-}^{13}\text{C}$] Gly and [$\text{U-}^{13}\text{C}$] Gly for examples of I - $S(1/2)$ systems; 2) glycine-2,2- d_2 and $\text{L-tyrosine-(phenyl-3,5-}d_2\text{)-HCl}$ for I - $S(1)$ systems; and 3) sodium tetraborate decahydrate and sodium citrate dehydrate for I - $S(3/2)$ spin systems. All samples were purchased from Sigma-Aldrich (St. Louis, MO) and used without further treatment except $\text{L-tyrosine-(phenyl-3,5-}d_2\text{)-HCl}$ that was dissolved in 1 M hydrochloric acid and recrystallized by slow evaporation before use. All experiments were carried out at room temperature, in 11.7 T and 14.1 T magnets equipped with Bruker Avance consoles operating at ^1H frequencies of 500.23 MHz and 600.92 MHz, respectively (^{13}C frequencies of 125.80 and 150.45 MHz, respectively). A 2.5 mm Bruker MAS NMR probe was used at 11.7 T for obtaining a moderate MAS rate, $\nu_r = 25\text{--}31$ kHz; a 1.3 mm Bruker MAS NMR probe at 14.1 T provided an "ultrafast" MAS rate, $\nu_r \geq 50$ kHz. About 2–3 mg and 7 mg of sample were packed into 1.3 mm and 2.5 mm Bruker MAS rotors, respectively. The swept RF pulse shapes were constructed by utilizing the shaped pulse tool of the Bruker Topspin[®] software. The WURST pulse employed in the BRAIN-CPMAS experiments utilized an amplitude-modulated profile $\nu_{1S}(1 - \cos^{40}[\pi t/\tau_p])$ and a phase modulation that results in a linear frequency sweep between 2000 data points were employed to digitize these WURST pulse shapes. Suitable frequency sweep windows ($\Delta\nu$) and CP mixing times (t_p) were chosen to cover ranges from 20 to 400 kHz and 2–14 ms, respectively. Optimal CP pulse parameters were found to be: 1) $\Delta\nu = 60\text{--}110$ kHz ($< 2\nu_r$) and $t_p = 10$ ms for ^{13}C -labeled compounds at $\nu_r = 60\text{--}65$ kHz; 2) $\Delta\nu = \nu_r = 60$ kHz and $t_p = 8$ ms for ^2H -labeled compounds at $\nu_r = 60$ kHz; 3) $\Delta\nu = 15$ kHz and $t_p = 8$ ms for ^{23}Na and ^{11}B experiments at $\nu_r =$

25–31 kHz. Optimal ^1H and S (^{13}C , ^2H , ^{23}Na , and ^{11}B) RF power conditions were sought experimentally by sweeping both RF channels independently and iteratively for 2 or 3 times.

For comparison, conventional CPMAS NMR experiments were also carried out with independent optimizations, employing either square-shaped or ramped (90%–110%) spin-lock pulses on the ^1H channel while simultaneously applying a rectangular spin-lock pulse on the S channel (^{13}C , ^2H , ^{23}Na , or ^{11}B). The mixing times used in these CPMAS experiments were between 0.5 and 2.5 ms, based on optimizations. All CP spectra were acquired by co-adding 4 transient signals with a 5 s recycle delay. SPINAL-64 [96] proton decoupling was used during the direct acquisition period, with a 100 kHz decoupling power. In addition, a low-power decoupling sequence, (XiX)₄₅ [97], was also utilized in 2D ^{13}C - ^{13}C EXSY experiments under ultrafast MAS spinning rates.

5. Results

The aim of our experiments was to verify the various phenomena introduced in Figs. 5–6, and in particular, the offset dependent, broadband BRAIN-CPMAS profile for each spin pair at fast spinning rates. For comparison, both BRAIN- and conventional ramped HH-CPMAS experiments were conducted at identical MAS spinning rates for a model compound, [$1\text{-}^{13}\text{C}$] Gly, under optimal ν_{1S} and ν_{1I} RF field strengths after individual optimizations. For optimizing RF pulse strengths for the BRAIN-CPMAS experiments, sets of ν_{1I} and ν_{1S} amplitudes were experimentally tested under a fixed set of $\Delta\nu$, t_p , and ν_r parameters, as shown in Fig. 7 (data for the RF field strength optimizations of the ramped HH-CPMAS experiments are not shown). In Fig. 7A, optimal ^{13}C and ^1H RF amplitudes for the $I(^1\text{H})$ - $S(^{13}\text{C})$ BRAIN-CPMAS experiment with $\nu_r = 65$ kHz were determined experimentally by independently varying ν_{1I} and ν_{1S} , while employing WURST pulse parameters $\Delta\nu = 110$ kHz and $t_p = 10$ ms ($\psi_0 = 0^\circ$). The y-axes of the various plots are scaled relative to the largest absolute magnitude, which is normalized to one. The optimal ^{13}C and ^1H RF fields (i.e., those yielding the largest signal) found were with $\nu_{1S}(^{13}\text{C}) = 45 \pm 4$ kHz and $\nu_{1I}(^1\text{H}) = 17 \pm 5$ kHz at $\nu_r = 65$ kHz, satisfying the DQ₁ CP mode ($\nu_{1H} + \nu_{eC} = \nu_r$). In a separate set of measurements employing a MAS rate of $\nu_r = 25$ kHz at 11.7 T, the optimal ^{13}C RF field was found at 20 kHz while the optimal ^1H RF fields were 42 kHz (ZQ₋₁; $\nu_{1H} = \nu_r + \nu_{eC}$) and 65 kHz (ZQ₋₂; $\nu_{1H} = 2\nu_r + \nu_{eC}$) (data not shown). In this case, the WURST pulse parameters employed for the experiments were $\Delta\nu = 48$ kHz and $t_p = 10$ ms ($\psi_0 = 0^\circ$). As can be deduced from these data, the ZQ CP mode is dominant at low MAS spinning rate, but when MAS spinning rate is increased, the DQ CP mode becomes dominant.

Fig. 7B shows the optimal $\nu_{1I}(^1\text{H})$ and $\nu_{1S}(^2\text{H})$ RF field strengths determined for the I - $S(1)$ BRAIN-CPMAS, using partially deuterated glycine-2,2- d_2 as a model compound. For $\nu_r = 60$ kHz, an optimal ^2H RF field ν_{1S} was found at 8 ± 4 kHz, when ν_{1H} was set at 47 ± 5 kHz with $\Delta\nu = \nu_r = 60$ kHz and $t_p = 8$ ms; this mode is also corresponds to the DQ₁ CP mode. Other CP modes are visible in the RF pulse sweep profiles, such as DQ₂ ($\nu_{1H} = 116 \pm 5$ kHz; $\nu_{1S} = 8 \pm 4$ kHz) and ZQ₋₁ ($\nu_{1H} = 78 \pm 5$ kHz; $\nu_{1S} = 8 \pm 4$ kHz); however, these are not as efficient as the DQ₁ mode. Fig. 7C shows the optimal $\nu_{1I}(^1\text{H})$ and $\nu_{1S}(^{11}\text{B})$ RF field strengths determined for $I(^1\text{H})$ - $S(^{11}\text{B})$ BRAIN-CPMAS, using sodium tetraborate decahydrate as a model compound. Under a moderately fast spinning rate of $\nu_r = 31$ kHz, an optimal ^{11}B RF field was found at 5 ± 3 kHz when $\nu_{1I}(^1\text{H})$ was set to 55 ± 2 kHz, with $\Delta\nu = 15$ kHz and $t_p = 4$ ms (this corresponds to the DQ₂ condition). Other modes visible in the $\nu_{1I}(^1\text{H})$ sweep profiles, such as DQ₁ ($\nu_{1I} = 26 \pm 3$ kHz; $\nu_{1S} = 5 \pm 3$ kHz), ZQ₋₁ ($\nu_{1I} = 35 \pm 3$ kHz; $\nu_{1S} = 5 \pm 3$ kHz) and ZQ₋₂ ($\nu_{1I} = 65 \pm 3$ kHz; $\nu_{1S} = 5 \pm 3$ kHz), were not as efficient as the DQ₂ mode.

The broadband nature of the BRAIN-CPMAS method was tested on an $I(^1\text{H})$ - $S(^{13}\text{C})$ system, and compared to a ramped HH-CPMAS pulse sequence at moderately fast and ultrafast MAS rates, while varying the ^{13}C offset frequencies (Ω_S), while using the optimal ν_{1H} and ν_{1C}

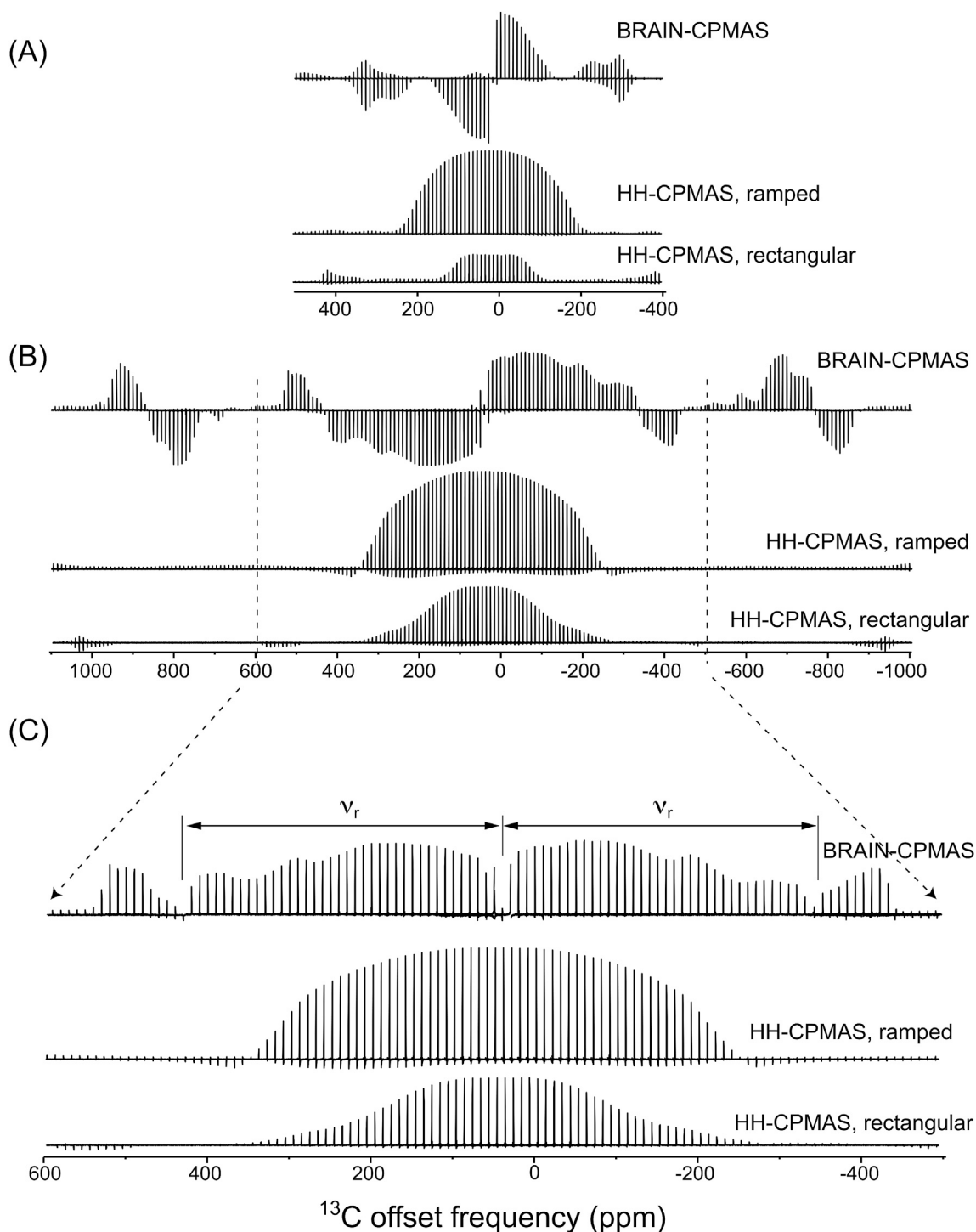


Fig. 8. Experimental Ω_C -dependent CP profiles of BRAIN- and conventional CPMAS methods measured on $[1-^{13}\text{C}]$ Gly at MAS rates of $\nu_r = 25$ kHz (A) and $\nu_r = 65$ kHz (B) with the optimized ν_{1C} and ν_{1H} values as shown in Fig. 7a: for BRAIN-CPMAS $\nu_{1H} = 17$ kHz and $\nu_{1C} = 45$ kHz in the case of $\nu_r = 65$ kHz, and $\nu_{1H} = 42$ kHz and $\nu_{1C} = 20$ kHz in the case of $\nu_r = 25$ kHz. For CPMAS, a separate optimization experiment was carried out for both rectangular version and a ramped version with a mixing time of 2 ms. The optimal HH-CPMAS conditions thus were found were: $\nu_{1H} = 112$ kHz (rectangular) and 148 kHz (ramped) in the case of $\nu_r = 65$ kHz; $\nu_{1H} = 44$ kHz (rectangular) and 82 kHz (ramped) in the case of $\nu_r = 25$ kHz. The same ν_{1C} (= 45 kHz) was used as the BRAIN-CPMAS method in each case of MAS rate. Spectra were collected in $\Delta\Omega_S = 1.5$ kHz (10 ppm) increments to simulate the effects of sites with varying offsets. Included in (C) are expanded versions of (B) to better view the central Ω_C range, with the BRAIN inset's negative peaks multiplied by -1 in order to better appreciate the CP dip.

conditions shown in Fig. 7A. As proof-of-principle, CPMAS performance was evaluated between -400 and $+500$ ppm ^{13}C offset ranges for $\nu_r = 25$ kHz, and between -1000 and $+1100$ ppm for $\nu_r = 65$ kHz. Spectra arising from BRAIN-CPMAS experiments on $[1-^{13}\text{C}]$ Gly under moderate ($\nu_r = 25$ kHz) and fast ($\nu_r = 65$ kHz) MAS rates, are shown in

Fig. 8A and B, respectively. A single vertical line in each profile corresponds to a CP spectrum measured at a particular ^{13}C frequency offset (spectra are free from CSA-derived spinning sidebands because of the fast MAS rates employed). Also included in Fig. 8A and B are the offset-dependent profiles of HH-CPMAS experiments based on the

conventional spin-lock pulse on the ^{13}C channel, while employing either a rectangular or ramped pulse on the ^1H channel. In these HH experiments, the same $\nu_{1\text{C}}$ value as in the BRAIN-CPMAS experiment was used, while employing an optimal $\nu_{1\text{H}}$ that was found by sweeping the latter's strength in the of 10–200 kHz range. It is clear that at moderate MAS rates ($\nu_r = 25$ kHz), the BRAIN-CPMAS method does not possess an advantage over conventional or ramped HH-CPMAS methods. However, when $\nu_r = 65$ kHz, the BRAIN-CPMAS method provides polarization transfers over a far broader range of frequency offsets (over 285 kHz in this case). For the central frequency region, the best CP modes correspond to DQ_1 , ZQ_{-1} , and ZQ_{-2} for the BRAIN-, rectangular HH-, and ramped HH-CPMAS experiments, respectively. The bandwidth of the DQ_1 mode in the BRAIN-CPMAS profile is about $2\nu_r$, which reaches 130 kHz when $\nu_r = 65$ kHz. Even if only this central DQ_1 mode is considered, the ensuing bandwidth of cross-polarization is far wider than what is achieved by the ramped HH-CPMAS method. The signal intensity of the DQ_1 mode of the BRAIN-CPMAS method is comparable to that of rectangular HH-CPMAS; although its bandwidth is narrower, the ramped HH-CPMAS method provides the highest signal intensity among all the cases for frequencies that are close to the on-resonance position. An interesting feature displayed by all the BRAIN-CPMAS profiles is the presence of an overall anti-symmetry about $\Omega_s \equiv 0$; this is due to the afore-mentioned

RR inversion effects that occur when the matching condition $\nu_{e\text{C}} = \nu_r$ is met. Fig. 8C shows a magnified view of the central portion of Fig. 8B, with the phases of peaks possessing reversed intensities in the BRAIN-CPMAS profile multiplied by -1 to better compare the overall profile to the HH-CPMAS results. It is worth noting that similar RR effects were also observed with other types of frequency-swept pulses, such as those featuring hyperbolic secant phase modulation [44].

For evaluating the effectiveness of the various ^1H - ^2H CPMAS methods, Fig. 9 compares BRAIN-CPMAS, ramped HH-CPMAS and directly excited ^2H spectra of glycine-2,2- d_2 with MAS rates of 40, 50 and 60 kHz. Also included for comparison on the bottom panels are ideal ^2H MAS lineshapes of a ^2H site simulated with $C_Q = 168$ kHz. Both BRAIN-CPMAS and ramped HH-CPMAS NMR spectra were acquired after optimizations of $\nu_{1\text{S}}$ and $\nu_{1\text{H}}$ for each spinning rate according to the strategy described in Fig. 7. The number shown beside each spectrum represents the relative integrated intensity of the isotropic centerband and spinning sideband manifolds, as compared to the DQ_1 mode spectrum arising from HH-CPMAS, whose centerband possesses the strongest intensity for every MAS rate and whose height has been used to normalize the intensities of all the remaining spectra. Notice that although both DQ_1 and ZQ_{-1} HH-CPMAS modes are included in this comparison, only the DQ_1 BRAIN-CPMAS condition is presented, as this provides the highest intensity

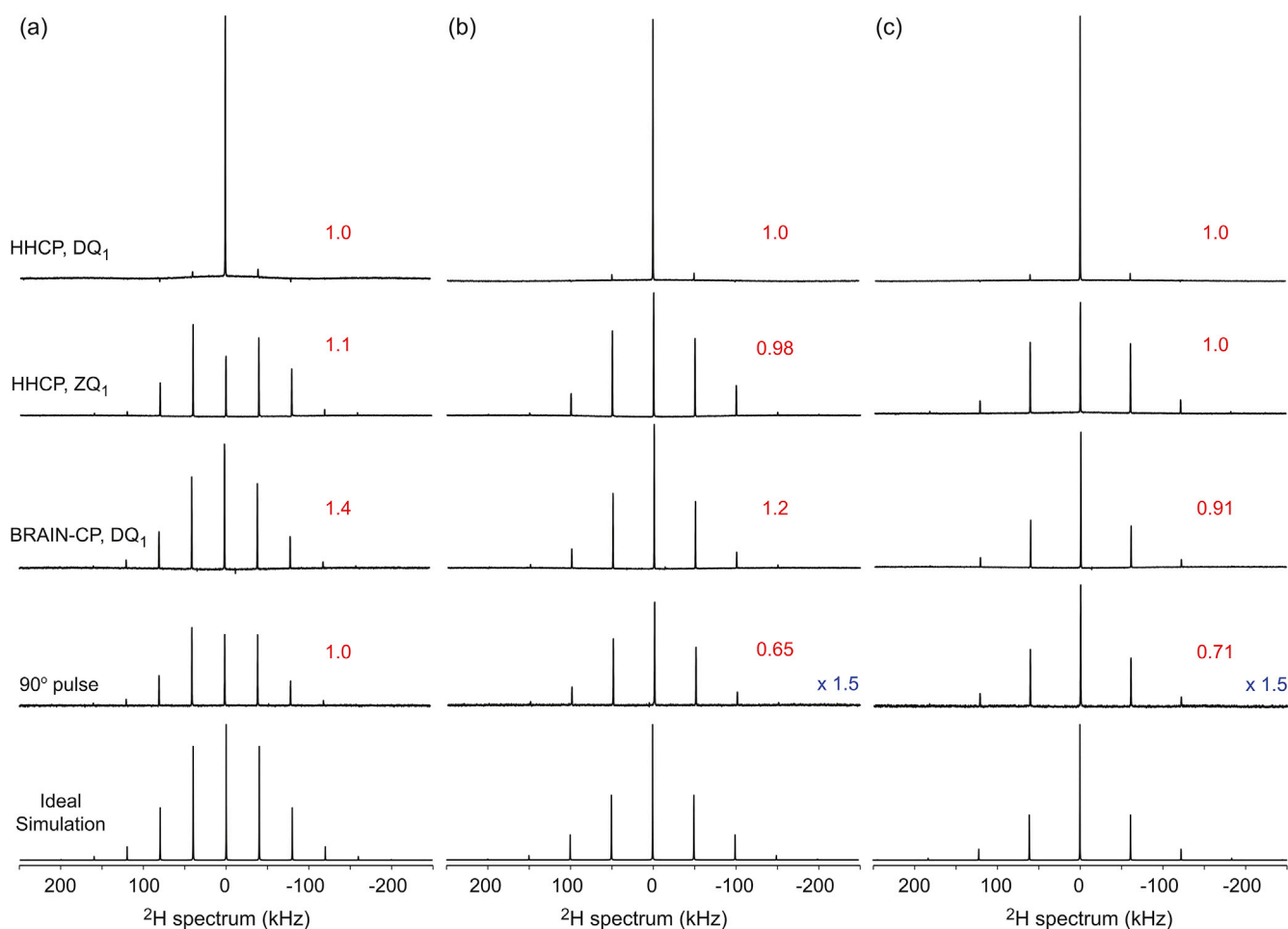
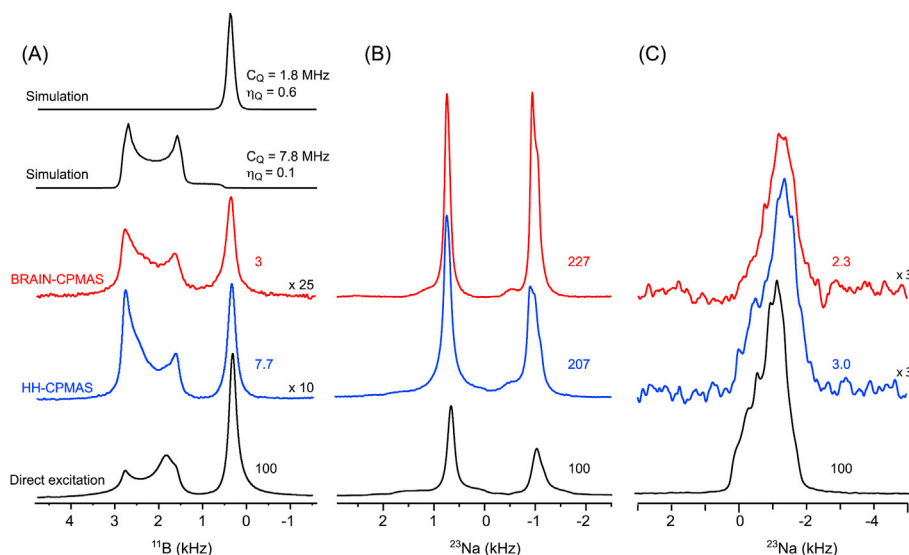


Fig. 9. BRAIN-CPMAS, ramped HH-CPMAS, and direct excitation MAS ^2H spectra of glycine-2,2- d_2 at spinning rates $\nu_r = 40$ (A), 50 (B) and 60 (C) kHz. Indicated for each rate are the CP modes involved, and (in red) the relative intensities of the integrated sideband manifolds. Except for the indicated 90° direct excitation panels, all spectra are shown with equally normalized vertical scales, for equal gains, and same number of scans. The bottom spectrum in each column is an ideal MAS lineshape simulated for the corresponding spinning rates. Every experimental spectrum was obtained by independently optimizing ^1H and ^2H RF fields. For instance, the RF fields for the DQ_1 BRAIN-CPMAS acquisition and for the ZQ_{-1} of HH-CPMAS spectrum at $\nu_r = 60$ kHz are as given in Fig. 7b; see text for additional details. The optimized condition, ZQ_{-1} mode, for the ramped HH-CPMAS experiment at $\nu_r = 60$ kHz was $\nu_{1\text{S}} = 73 \pm 4$ kHz and $\nu_{1\text{H}} = 130 \pm 5$ kHz with a mixing time of 2 ms. All experimental spectra were obtained by coadding 128 transients with a 4 s recycling delay. (For interpretation of the references to color in this figure legend, the reader is referred to the Web version of this article.)



and best lineshape, even while employing the smallest ^2H RF amplitudes. Features to notice from these comparisons are: (i) The centerband obtained from HH-CPMAS DQ_1 mode is the highest at every ν_r , and although this does not hold when considering the overall integrated intensity from the isotropic centerband and spinning sidebands, the spectrum's appearance is dominated the isotropic centerband only. (ii) The BRAIN-CPMAS DQ_1 condition yields MAS sideband patterns at every spinning rate that are in excellent agreement with ideal simulations; the experimental conditions in each case feature relatively small ^1H and ^2H RF fields (e.g., $\nu_{1S} = 8 \pm 4$ kHz and $\nu_{1H} = 47 \pm 4$ kHz for $\nu_r = 60$ kHz). (iii) Although the ZQ_1 mode of HH-CPMAS method also provides an MAS sideband pattern that matches relatively well with simulations, it does so at the expense high RF amplitudes for both ^1H and ^2H channels (e.g., $\nu_{1S} = 73 \pm 4$ kHz and $\nu_{1H} = 130 \pm 5$ kHz for $\nu_r = 60$ kHz).

Fig. 10 compares BRAIN-CPMAS, ramped HH-CPMAS and directly-excited (a) ^{11}B and (b) ^{23}Na MAS spectra of sodium tetraborate decahydrate, and (c) ^{23}Na MAS spectra of citrate dihydrate. The number next to each spectrum represents the relative peak intensity of the spectrum. The peak intensity of the directly excited spectrum was set at 100 for each nuclide, and the peak intensities of the other spectra obtained by the BRAIN-CPMAS and HH-CPMAS methods are compared with respect to this directly excited spectrum. When two peaks occur in one spectrum, they are described based on the intensity of the larger peak. Among many different CP modes producing signals in the BRAIN-CPMAS and HH-CPMAS spectra, only those yielding the highest intensities are included in these comparisons: for instance, DQ_2 for BRAIN-CPMAS and ZQ_2 for HH-CPMAS in (A). Also included in the top two rows in Fig. 10A are simulations of the idealized quadrupolar patterns based on the known parameters ($C_Q = 1.8$ MHz, $\eta_Q = 0.6$; $C_Q = 7.8$ MHz, $\eta_Q = 0.1$) [98]. A good match between experiment and simulation is observed for the BRAIN-CPMAS spectrum in (A), which has lower SNR but fewer distortions than its ramped HH-CPMAS counterpart. Also note that the ^1H and ^2H RF amplitudes are very small for this BRAIN-CPMAS spectrum ($\nu_{1H}[^1\text{H}] = 55$ kHz; $\nu_{1S}[^{11}\text{B}] = 5$ kHz) in comparison to those used in the HH-CPMAS case. From the spectra shown in Fig. 10B and C, the relative increases in signal intensity in the BRAIN- and HH-CPMAS spectra are comparable. Furthermore, both BRAIN-CPMAS and HH-CPMAS spectra of sodium tetraborate decahydrate possess higher signal intensities than their directly polarized counterpart, in accordance with the observations by Harris and Nesbitt [98].

To further evaluate these experiments, offset- (Ω_S -) dependent 2D BRAIN-CPMAS and HH-CPMAS profiles were numerically simulated,

Fig. 10. BRAIN-CPMAS (red), ramped CPMAS (blue), and direct excitation (black) MAS ^{11}B and ^{23}Na spectra of sodium tetraborate decahydrate and ^{23}Na spectra of citrate dehydrate at spinning rates $\nu_r = 31$ kHz and 25 kHz, respectively. The experimental parameters used for BRAIN-CPMAS in each case are: (A) the same parameters as introduced in Fig. 7c; (B) $t_p = 4$ ms, DQ_1 mode ($\nu_{1S} = 14$ kHz, $\nu_{1H} = 4.7$ kHz); (C) $t_p = 2$ ms, ZQ_2 mode ($\nu_{1S} = 30$ kHz, $\nu_{1H} = 85$ kHz). The experimental parameters used for the ramped HH-CPMAS were based on individual optimizations in each case (conditions are not shown). Directly excited ^{11}B and ^{23}Na MAS spectra were also acquired via the application of a 90° pulse on the S-channel (^{11}B and ^{23}Na) and subsequent ^1H decoupling (bottom spectra in black color in each column). The relative signal intensities are indicated by the numbers, established by placing the signal intensity of the directly excited spectrum as 100. Every spectrum was obtained by coadding 1024 transients with a 30 s recycle delay. Simulations of ideal spectra are included in the top two rows in (A). (For interpretation of the references to color in this figure legend, the reader is referred to the Web version of this article.)

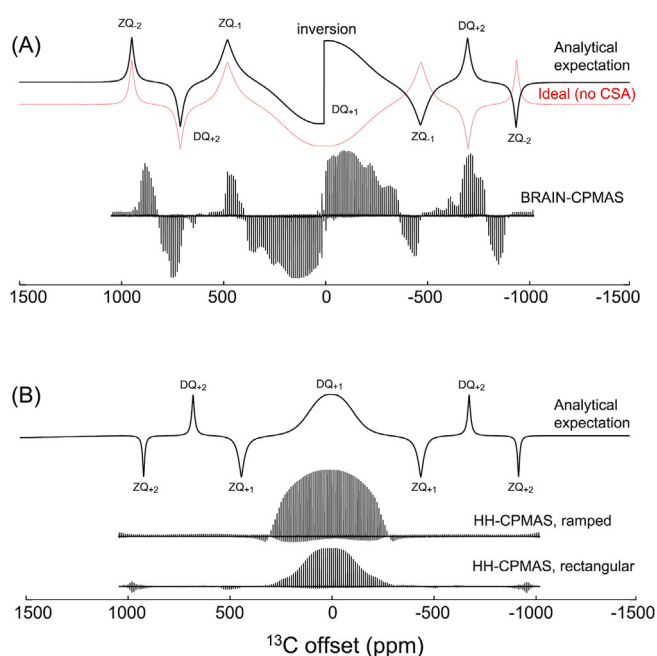


Fig. 11. Comparisons between the experimental and theoretical Ω_C -dependent CP profiles observed for $[1-^{13}\text{C}]$ Gly from the BRAIN- (A) and conventional CPMAS (B) experiments measured at a MAS rate $\nu_r = 65$ kHz. The theoretical profiles in (A) and (B) show cross-sections taken at the optimal ν_{1C} values from the corresponding 2-dimensional (2D) Ω_C - ν_{1C} map taken at $\nu_{1C} = 37.2$ kHz and $\nu_{1C} = 48$ kHz, respectively, that match the DQ_1 mode of each case at the central region, with $\nu_{1H} = 17$ kHz and $\nu_r = 65$ kHz (tensor parameters employed in both simulations were: $b_{IS} = 23$ kHz; $\delta_{CSA} = 40$ ppm, $\eta_{CSA} = 0.3$). Experimental CPMAS profiles are taken from Fig. 8b. The theoretical profile shown in (A) with a red line depicts the theoretical BRAIN-CPMAS profile expected when neglecting CSA-driven RR effects. Both the experimental and simulated spectra of the BRAIN-CPMAS case shown in (A) are the same DQ_1 mode. However, the experimental HH-CPMAS spectra that were compared to the simulated DQ_1 mode in (B) correspond to ZQ_1 (rectangular; $\nu_{1H} = 112$ kHz, $\nu_{1C} = 48$ kHz) and ZQ_2 (ramped; $\nu_{1H} = 148$ kHz, $\nu_{1C} = 48$ kHz) modes that were found independently by experimental optimizations. (For interpretation of the references to color in this figure legend, the reader is referred to the Web version of this article.)

seeking their variation with ν_{1S} (along the horizontal x-axis) and with Ω_S (in the vertical-y axis). Then, an 1D slice can be taken at a specified ν_{1S} -value from a 2D ν_{1S} - Ω_S plot, and compared with experimental BRAIN- or HH-CPMAS profiles [68]. For the simplest $I(1/2)$ - $S(1/2)$ case, these experimentally obtained offset-frequency profiles could be compared against analytical predictions arising from the average Hamiltonian theory described in Section 3.6. Shown in Fig. 11A is the 1D slice calculated analytically by employing $\nu_{1H} = 17$ kHz, 37 kHz $\leq \nu_{1C} \leq 42$ kHz, and $\nu_r = 65$ kHz, compared against the experimental BRAIN-CPMAS profile measured for $[1-^{13}\text{C}]$ Gly (see Fig. 8B). Shown in Fig. 11B is a comparison of experimentally obtained ramped and rectangular HH-CPMAS profiles with the simulated Ω_S -dependent CP profile expected under a HH match with an optimized value of $\nu_{1C} = 48$ kHz, $\nu_{1H} = 17$ kHz and $\nu_r = 65$ kHz. As can be seen from Fig. 11A, the CP model introduced earlier together with the RR inversion explains the overall shape and frequency positions of the Ω_S -dependent CP profile.

Fig. 12A shows the offset dependence of the BRAIN-CPMAS pulse sequence, as explored by collecting a series of spectra under DQ_1 matching conditions when $\Omega_S = 0$, as a function of the ^2H centerband offset vs. the width of the adiabatic pulse sweep. Three different spinning

rates ($\nu_r = 40, 55,$ and 60 kHz) were utilized, while setting $\Delta\nu = \nu_r$ in order to satisfy a “single spinning sideband sweep” situation that is free from the destructive interferences introduced in Fig. 1. Remarkably, for every ν_r , “modes” arise where peaks change their signs as the frequency is swept, with the width of each mode spanning $\sim 0.5\nu_r$; these sign changes are influenced solely by the effective offset between the centerband and the center of the WURST pulse. All these offset dependencies are nearly symmetric with respect to the $\Omega_S = 0$ position. These periodic inversions cannot be entirely ascribed to RR phenomena, as no such effects are expected over the offset range $-\frac{\nu_r}{2} \leq \Omega_S/2\pi \leq +\frac{\nu_r}{2}$ for the small values of ν_{1S} , while the first inversions are observed at $|\Omega_S/2\pi| \approx \frac{\nu_r}{4}$. The origin of these sign changes in the experimental spectra acquired at different offset frequencies can be heuristically understood by investigating the offset-swept profile of time-dependent ZQ- and DQ-CP matching conditions. Fig. 12B illustrates the time-dependent HH matching conditions that are satisfied by the $\text{DQ}_1, \text{DQ}_2, \text{ZQ}_0, \text{ZQ}_{-1},$ and ZQ_{-2} BRAIN-CPMAS modes, during the course of an 8 ms WURST-40 pulse. As derived in Eqs. (54) and (55), these conditions are given as $\nu_{1I} - \nu_{eS}(t) = 0$ and $\nu_{1I} \mp \nu_{eS}(t) \pm k\nu_r = 0$. Also shown in Fig. 12B are the positions where RR conditions arise as a function of carrier offset Ω_S and of the contact time. Notice that

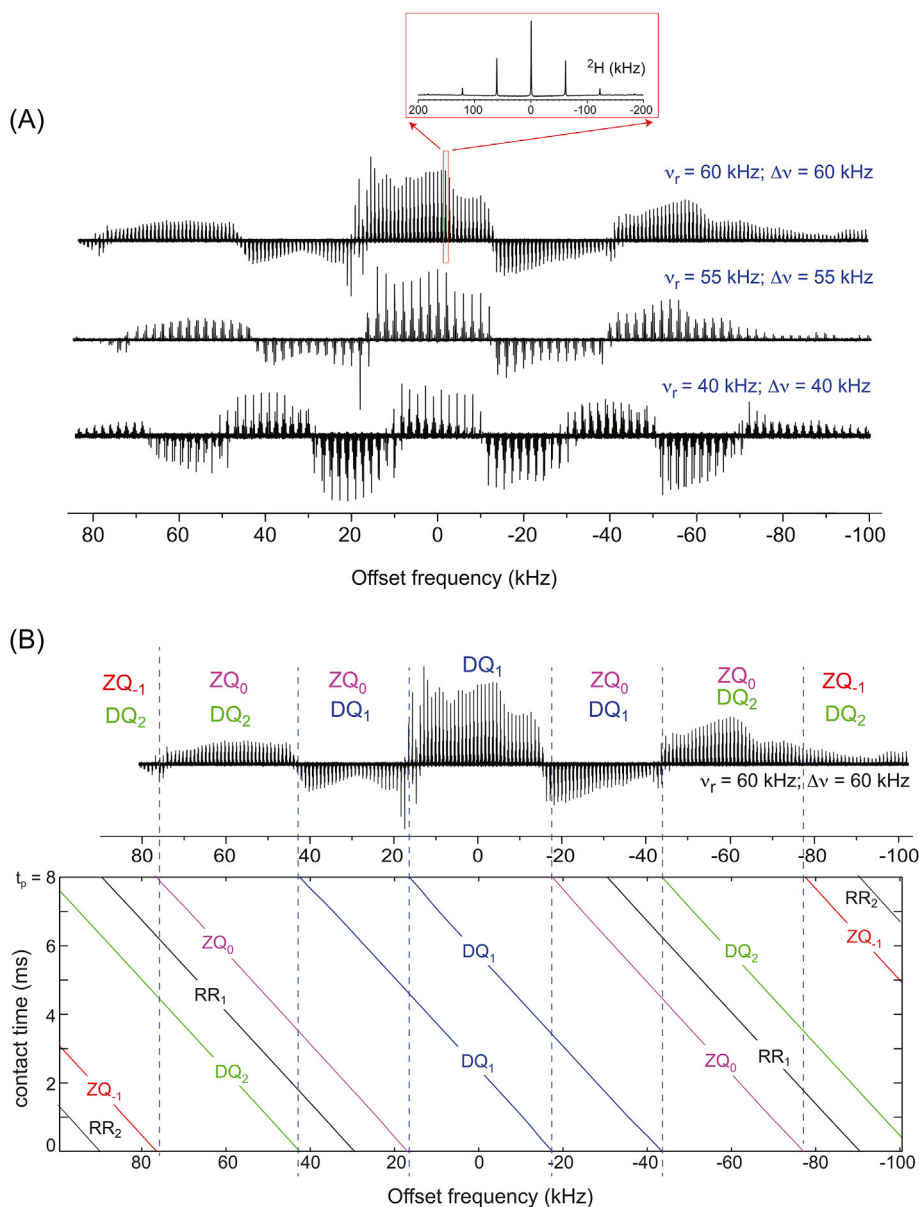


Fig. 12. (A) Influence of the isotropic ^2H offset on the BRAIN-CPMAS performance for different spinning rates. Experimentally CP-enhanced profiles of the ^2H polarizations were measured on glycine-2,2- d_2 by varying the central carrier Ω_S of the adiabatic sweeps involved, with individually optimized ν_{1S} and ν_{1I} values. The sweep frequency span $\Delta\nu$ was matched to the MAS rate ν_r in each case. Each Ω_S -varied CP-enhanced profile shown consists of an entire BRAIN-CPMAS ^2H spectrum measured at a specific Ω_S value, as illustrated by the inset figure (corresponding to a spectrum measured at $\Omega_S/2\pi = -4$ kHz with $\nu_r = \Delta\nu = 60$ kHz, $\nu_{1S} = 5$ kHz and $\nu_{1H} = 47$ kHz). Offset increments of 1–2 kHz were used to record the entire sets of experiments. Notice the spectral sign inversions observed around the central on-resonance frequency position, at offsets within the range $-0.25\nu_r \leq \frac{\Omega_S}{2\pi} \leq 0.25\nu_r$. (B) Analysis of the experimentally observed periodic magnetization inversions observed using BRAIN-CPMAS on a glycine-2,2- d_2 sample, and the time-dependent fulfillment of DQ_1 (blue line), DQ_2 (green line), ZQ_0 (purple), ZQ_{-1} (red), and RR (black) matching conditions, within a HH process involving a linearly-chirped pulse lasting for a duration t_p . Plots are shown as a function of offset frequency $\Omega_S/2\pi$. The Ω_S -varied CP-enhanced profile analyzed in (B) is the $\nu_r = \Delta\nu = 60$ kHz case in (A). (For interpretation of the references to color in this figure legend, the reader is referred to the Web version of this article.)

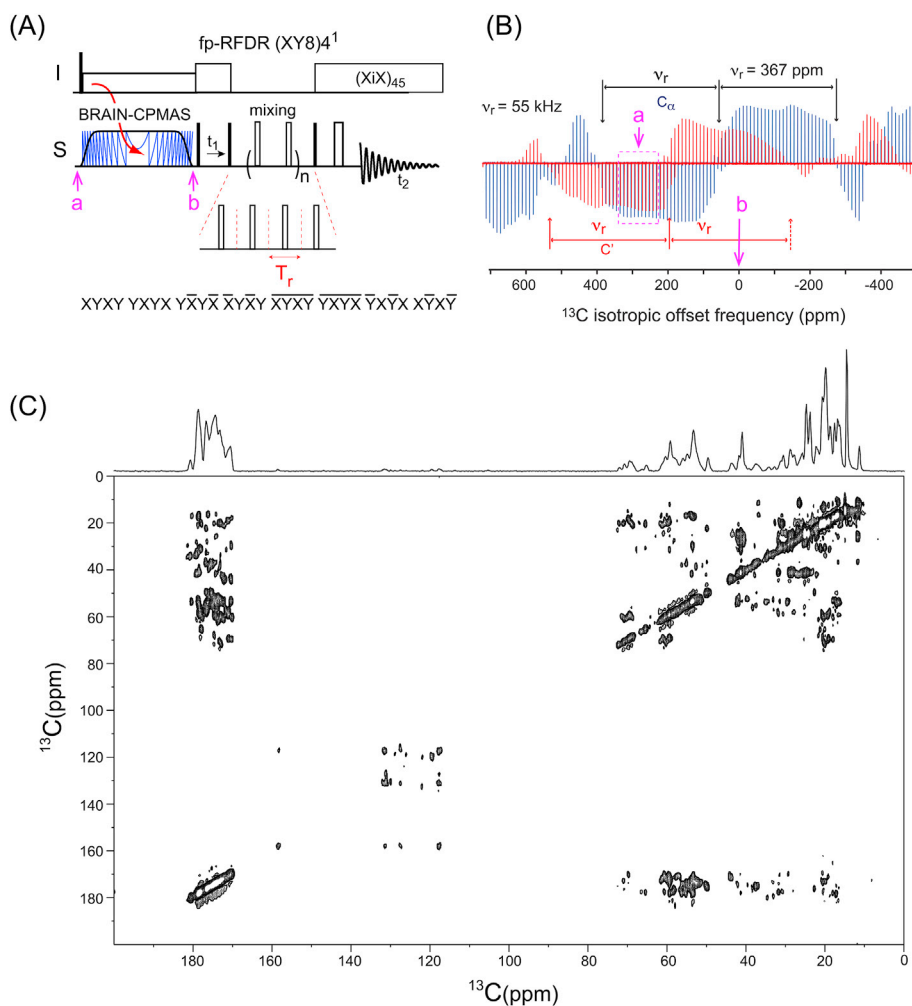


Fig. 13. An offset-frequency jump scheme of 2D ¹³C-¹³C exchange spectroscopy utilizing the BRAIN-CPMAS-based fp-RFDR(XY8)₄ mixing scheme. (A) A pulse scheme of the 2D homonuclear dipolar correlation experiment that combines the BRAIN-CPMAS sequence with the fp-RFDR(XY8)₄ pulse scheme. The pulse phases used in the fp-RFDR(XY8)₄ mixing scheme shown in the figure. Marked by “a” and “b” in pink color in the pulse sequence denote offset jump positions for off-resonance and on-resonance irradiation, respectively, for obtaining a 2D exchange spectrum with all in-phase peaks. (B) An offset-frequency swept CP profile measured on [U-¹³C] Gly measured at 14.1 T (Δν = 70 kHz, t_p = 10 ms) under ν_r = 55 kHz. Signals in red and blue are for carbonyl carbon and C_α, respectively, obtained by varying the offset frequency for the BRAIN-CPMAS mixing. Each line corresponds to the sideband-free center peak of the corresponding ¹³C signal. The DQ₁ mode of each site that spans about 2ν_r, with a central RR inversion, is indicated. Note the spectral region in the dashed rectangle (in pink) with the same signal phase for both C' and C_α peaks to which the offset frequency can be jumped during the BRAIN-CPMAS block in the sequence shown in (A) for obtaining all positive signals in the 2D spectrum. (C) 2D ¹³C-¹³C spectrum, with all positive diagonal and cross peaks, measured on [U-¹³C] GB1 at 14.1 T under a MAS spinning rate ν_r = 55 kHz employing an offset jump scheme with a = 240 ppm and b = 0 ppm (110 ppm from TMS was considered as the on-resonance position; Δν = 70 kHz, t_p = 10 ms). (For interpretation of the references to color in this figure legend, the reader is referred to the Web version of this article.)

for small offsets and sweeps spanning a range $\leq \Delta\nu$ two different lines for each CP mode are present due to the quadratic dependence of $v_{eS}(t)$ on the sweep's offset – even if only one of these will be associated with a significant $I \rightarrow S$ polarization transfer, as discussed for Fig. 5B above. Fig. 12B was derived assuming $\Delta\nu = \nu_r = 60$ kHz, $\nu_{1S} = 5$ kHz, and $\nu_{1H} = 47$ kHz; the experimental offset-swept spectrum shown in Fig. 12A, collected employing the same experimental parameters, is shown for purposes of comparing the frequency positions of the sign inversions. From this, it appears that the changes in the S -spin polarization arising at $|\Omega_s/2\pi| \approx \nu_r/4, 3\nu_r/4, \text{ and } 5\nu_r/4$, coincide with a change in the CP mode that is affecting the transfer – from DQ to ZQ, and vice versa. Indeed, all spectral sign changes coincide with the starting or ending of one of these CP modes. This is reasonable, as these CP modes will polarize S_z in opposite directions – cf. Eqs. (61)–(64). Furthermore, it appears that when multiple potential CP modes can become active over the course of the contact time for a particular Ω_s offset value, one of them usually dominates the sign of the resulting S -magnetization. Moreover, much weaker effects are observed here upon traversing a RR condition than in the case of BRAIN-CPMAS for a $I \rightarrow S(1/2)$ system, apparently due to the higher efficiency of RR processes when CSA is present [28].

The presence of a central RR inversion results in negative peaks along one side in the offset-frequency profile ($\Omega_s \leq 0$). This is an undesirable that can be corrected by post-processing, or experimentally addressed using an offset-frequency jump scheme whereby the off-resonance frequency position of the chirp is optimized for obtaining all peaks with the same phase following the mixing. The way in which this can be implemented is illustrated using the 2D ¹³C-¹³C exchange spectroscopy (EXSY)

sequence shown in Fig. 13A, formed by combining the BRAIN-CPMAS scheme with the fp-RFDR(XY8)₄ sequence [99]. An off-resonance frequency jump (240 ppm; 350 ppm from TMS) was applied at position “a” before the BRAIN-CPMAS sequence, as both the C' and C_α peaks of [U-¹³C] Gly, which was used as an external standard and for calibration, exhibit the same phase (Fig. 13B). Then, another frequency jump to an on-resonance position (110 ppm from TMS) is made to position “b” before entering the RFDR mixing block to obtain a 2D correlation resembling the usual on-resonance situation. A model protein, [U-¹³C] GB1, was employed for demonstrating the functionality of this offset-frequency jump scheme (BRAIN-CPMAS: ν_r = 55 kHz, Δν = 70 kHz, t_p = 7 ms; RFDR mixing time = 14 ms). As is identified from the 2D ¹³C-¹³C correlation spectrum shown in Fig. 13C, all peaks along both frequency domains are positively absorptive, as expected.

6. Discussion and conclusions

The features and properties of the BRAIN-CPMAS method as applied to polarization transfers between an $I = 1/2$ nuclide and $S = 1/2, 1$ or $3/2$ nuclide, were summarized herein. Particular emphasis was given to the possibility of polarizing bandwidths that are much larger than the applied RF fields, by employing adiabatic passage schemes covering a wide frequency range of Ω_s -offsets under fast MAS. In exploring this approach, some similarities with the static BRAIN-CP are noted; however, there are numerous differences in the two classes of experiments, largely due to MAS-driven effects. Some new features are expected MAS-induced aspects, like the need to contend with new ν_r-dependent DQ and

ZQ matching conditions arising during a frequency-swept pulse. Other features include coherent adiabatic/sudden passage phenomena of the kind taught to us by Lex Vega, including level crossings in half-integer quadrupoles, and rotary resonance phenomena driven by CSA or quadrupolar couplings. New phenomena are also explored, including a static-like ZQ₀ matching condition, driven by MAS-modulated quadrupolar-RF dipolar recoupling effects (this is clearly visible for the $S = 1$ case). From the standpoint of new phenomena, the RR effects were arguably the most interesting features noticed in these studies. Rotary resonances have been known to arise when an anisotropic shift or quadrupolar interaction is modulated by an MAS process at a spinning rate ν_r , and a magnetization that has been spin-locked by a field $\|\nu_{IS}\| = \nu_r, 2\nu_r$ [100–102]. This condition leads to a rapid dephasing of the spin-locked polarization, which can be visualized in a tilted rotating frame where the spin-locking RF takes the role of a Zeeman-like field, and the CSA- or quadrupolar-driven time modulation is akin to an oscillating transverse field. In this scenario, the “Zeeman field” is constant; however, when it becomes resonant with the transverse oscillations, the magnetization “tilts away” from the direction of the ν_{IS} spin-locking field. Furthermore, this evolution is orientation-dependent, depending upon the magnitude of the anisotropic CS or quadrupolar interactions; for a powder sample with many crystallite orientations, this leads to dephasing of the originally spin-locked magnetization. The case of a frequency swept pulse (i.e., WURST pulse), by contrast, leads to a different scenario, whereby the “Zeeman” field is slowly swept through resonance as the offset of the RF pulse changes. Given the relatively slow sweep rates involved in this passage, the effective field that is now relevant for defining the rotary resonance conditions always manages to invert the spin-locked polarization as the field transverses through the $\|\nu_{eS}\| = \nu_r, 2\nu_r$ RR conditions, provided that conditions of adiabaticity are met. This implies that the actual size of the “transverse” CSA or $H_Q^{(1)}(t)$ field does not matter, as it will effectively lead to an inversion of the spin-locked magnetization for all orientations – even when the CSA is too small to manifest in the NMR spectrum due to the application of relatively fast MAS rates. As such, this leads to homogeneous inversions of signal over broad bandwidths without dephasing, as was observed in both experiments and simulations.

All of these effects, as well as the matching conditions of the ZQ- and DQ CP modes in the BRAIN-CPMAS schemes, are accurately predicted by an average Hamiltonian model specifically developed to analyze the BRAIN-CPMAS experiment. The various predictions and phenomena described in this study on the basis of time-averaged Hamiltonian theories and of numerical simulations, coincided well with experiments on model samples. In general, we observed that under fast spinning rates, BRAIN-CPMAS presents advantages over conventionally ramped HH-CPMAS for achieving transfers over wide frequency ranges with low RF powers, but the method loses its advantage at lower MAS rates (e.g., <15 kHz).

For the I - $S(1/2)$ CP case, an enhancement profile spanning in excess of 285 kHz was measured with the BRAIN-CPMAS method on [^{13}C] Gly. This is an unprecedented frequency span for a HH transfer, and is particularly remarkable in light of the low RF amplitudes that were used on both the I - and S -channels. Even the width of the single DQ₁ CP mode, the most practically useful mode of the BRAIN-CPMAS method, reached ca. 130 kHz; this is ca. twice the polarizing window experimentally obtained by the ramped HH-CPMAS method (75 kHz). Moreover, the magnitude of the central DQ₁ mode transfer in the BRAIN-CPMAS method becomes larger as the MAS rate increases. Thus, BRAIN-CPMAS promises to become an even more attractive method for obtaining broadband CP transfers for nuclei possessing large chemical shift dispersions and anisotropies at fast MAS rates.

BRAIN-CPMAS can also be applied to I - $S(1)$ spin systems, delivering undistorted ^2H MAS NMR lineshapes with high SNR with the application of low RF amplitudes. This probably reflects the larger range of HH conditions that can be satisfied by a frequency-swept pulse for multiple

crystallites in a powder in comparison to its rectangular-wave counterpart. Based on repeated experiments, it appears that the optimal sweep width $\Delta\nu$ for the WURST pulse used in these I - $S(1)$ BRAIN-CPMAS experiments is one set equal to ν_r . Under such conditions, the HH-matching conditions become robust, and are satisfied regardless of the values of the quadrupolar coupling constants. However, ^1H - ^2H BRAIN-CPMAS experiments also have a number of limitations and complications. One concern is the complex polarization behavior shown in Fig. 12, which involves multiple sign changes of the peaks as a function of carrier offset frequency, Ω_S . From a practical standpoint, however, these are not terribly problematic, given the relatively narrow chemical shift range and small quadrupolar interactions associated with a spin-1 nucleus like ^2H . These considerations may become increasingly problematic for other integer spin nuclides like ^{14}N ($S = 1$) or ^{10}B ($S = 3$).

The performance of the BRAIN-CPMAS, in terms of maximizing polarization transfer an resultant S -spin signal, was the poorest for $I \rightarrow S(\geq 3/2)$ systems. This is largely due to quadrupolar-driven level crossings that, as in conventional CPMAS NMR [75,76], disrupt the spin-lock associated with the transition one is attempting to polarize (in this case, the CT). The use of a frequency-swept pulse further complicates matters, since this will simultaneously overlap with multiple central and satellite spinning sideband manifolds, which further decreases the spin-locking efficiency (Fig. 3). Optimized BRAIN-CPMAS conditions lead to ν_{IS} fields that are smaller than their HH counterparts; the quadrupolar-driven level crossing effects associated with spin-locking a central $+1/2 \leftrightarrow -1/2$ transition [43,49], are thus minimized. Moreover, small ν_{IS} fields yield nearly ideal spectral lineshapes for the central transition spectrum, but then often have lower SNR than their directly excited counterparts. The optimal solution for polarizing these species – the challenge first thrown to us by Vega’s pioneering work – thus still stands.

Acknowledgments

This work was supported by the NHMFL through the National Science Foundation Cooperative Agreement (DMR-1157490 and 1644779) and by the State of Florida. L.F. acknowledges support from the Israel Science Foundation grant 795/13, the Kimmel Institute for Magnetic Resonance (Weizmann Institute), and the generosity of the Perlman Family Foundation. R.W.S. thanks NSERC for funding this research in the form of a Discovery Grant and Discovery Accelerator Supplement, and is also grateful for a 50th Anniversary Golden Jubilee Chair from the University of Windsor.

References

- [1] E.R. Andrew, A. Bradbury, R.G. Eades, *Nature* 182 (1958) 1659.
- [2] I.J. Lowe, *Phys. Rev. Lett.* 2 (1959) 285.
- [3] U. Haeberlein, J.S. Waugh, *Phys. Rev.* 175 (1968) 453.
- [4] J.S. Waugh, L.M. Huber, U. Haeberlein, *Phys. Rev. Lett.* 20 (1968) 180.
- [5] R.G. Griffin, *Nat. Struct. Mol. Biol.* 5 (1998) 508.
- [6] H.J.M. de Groot, *Curr. Opin. Struct. Biol.* 10 (2000) 593.
- [7] R. Tycko, *Annu. Rev. Phys. Chem.* 52 (2001) 575.
- [8] F. Castellani, B. van Rossum, A. Diehl, M. Schubert, K. Rehbein, H. Oshikinat, *Nature* 420 (2002) 98.
- [9] A.E. McDermott, *Curr. Opin. Struct. Biol.* 14 (2004) 554.
- [10] T. Gullion, J. Schaefer, *J. Magn. Reson.* 81 (1989) 196.
- [11] H.W. Spiess, K. S.-R, *Multidimensional Solid-state NMR and Polymers*, Academic Press, 1994.
- [12] J. Schaefer, E.O. Stejskal, *J. Am. Chem. Soc.* 98 (1976) 1031.
- [13] E.O. Stejskal, J. Schaefer, J.S. Waugh, *J. Magn. Reson.* 28 (1977) 105.
- [14] R.L. Cook, C.H. Langford, R. Yamdagni, C.M. Preston, *Anal. Chem.* 68 (1996) 3979.
- [15] M. Sardashti, G.E. Maciel, *J. Magn. Reson.* 72 (1987) 467.
- [16] R. Wind, S.F. Dec, H. Lock, G.E. Maciel, *J. Magn. Reson.* 79 (1988) 136.
- [17] B.H. Meier, *Chem. Phys. Lett.* 188 (1992) 201.
- [18] X. Wu, K.W. Zilm, *J. Magn. Reson. A* 104 (1993) 154.
- [19] S.R. Hartmann, E.L. Hahn, *Phys. Rev.* 128 (1962) 2042.
- [20] A. Pines, M.G. Gibby, J.S. Waugh, *J. Chem. Phys.* 59 (1973) 569.
- [21] I.R. Dixon, M.D. Bird, J.R. Miller, *IEEE Trans. Appl. Supercond.* 16 (2006) 981.
- [22] I.R. Dixon, T. Adkins, H. Ehmeler, W.S. Marshall, M.D. Bird, *IEEE Trans. Appl. Supercond.* 23 (2013) 4300204.

- [23] S. Laage, J.R. Sachleben, S. Steuernagel, R. Pierattelli, G. Pintacuda, L. Emsley, *J. Magn. Reson.* 196 (2009) 133.
- [24] A. Lange, I. Scholz, T. Manolikas, M. Ernst, B.H. Meier, *Chem. Phys. Lett.* 468 (2009) 100.
- [25] S.M. Zhang, C.L. Czekaj, W.T. Ford, *J. Magn. Reson. A* 111 (1994) 87.
- [26] S. Hediger, B.M. Meier, R.R. Ernst, *Chem. Phys. Lett.* 213 (1993) 627.
- [27] S. Hediger, B.H. Meier, N.D. Kurur, G. Bodenhausen, E.R. R. Chem. Phys. Lett. 223 (1994) 283.
- [28] S. Hediger, B.H. Meier, R.R. Ernst, *Chem. Phys. Lett.* 240 (1995) 449.
- [29] W.K. Peng, K. Takeda, M. Kitagawa, *Chem. Phys. Lett.* 417 (2006) 58.
- [30] J.-P. Demers, V. Vijayan, S. Becker, A. Lange, *J. Magn. Reson.* 205 (2010) 216.
- [31] S. Jain, M. Bjerring, N.C. Nielsen, *J. Phys. Chem. Lett.* 3 (2012) 703.
- [32] A.C. Kolbert, A. Bielecki, *J. Magn. Reson. A* 116 (1995) 29.
- [33] A. Samoson, T. Tuherm, J. Past, *J. Magn. Reson.* 149 (2001) 264.
- [34] A. Wickramasinghe, S. Wang, I. Matsuda, Y. Nishiyama, T. Nemoto, Y. Endo, *Solid State Nucl. Mag.* 72 (2015) 9.
- [35] R. Fu, P. Pelupessy, G. Bodenhausen, *Chem. Phys. Lett.* 264 (1997) 63.
- [36] A.J. Vega, in: D.M. Grant, R.K. Harris (Eds.), *Encyclopedia of Nuclear Magnetic Resonance*, J. Wiley, Chichester, 1996, p. p 3869.
- [37] E. Kupce, R. Freeman, *J. Magn. Reson. A* 115 (1995) 273.
- [38] M.R. Bendall, *J. Magn. Reson. A* 112 (1995) 126.
- [39] T.-L. Hwang, M. Garwood, A. Tannús, P.C.M. van Zill, *J. Magn. Reson. A* 121 (1996) 221.
- [40] J. Baum, R. Tycko, A. Pines, *Phys. Rev. A* 32 (1985) 3435.
- [41] R.J. Ordidge, M. Wylezinska, J.W. Hugg, E. Butterworth, F. Franconi, *Magn. Reson. Med.* 36 (1996) 562.
- [42] J. Shen, *J. Magn. Reson. B* 112 (1996) 131.
- [43] D. Rosenfeld, S.L. Panfil, Y. Zur, *J. Magn. Reson.* 129 (1997) 115.
- [44] M. Garwood, L. delaBarre, *J. Magn. Reson.* 153 (2001) 155.
- [45] M.S. Silver, R.I. Joseph, D.I. Hoult, *J. Magn. Reson.* 59 (1984) 347.
- [46] M.S. Silver, R.I. Joseph, D.I. Hoult, *Phys. Rev. A* 31 (1985) 2753.
- [47] J. Pfeuffer, I. Tkac, I.-Y. Choi, H. Merkle, K. Ugurbil, M. Garwood, R. Gruetter, *Magn. Reson. Med.* 41 (1999) 1077.
- [48] H. Barfuss, H. Fischer, D. Hentschel, R. Ladebeck, A. Oppelt, R. Wittig, *NMR Biomed.* 3 (1990) 31.
- [49] A. Abragam, *Principles of Nuclear Magnetism*, Oxford University Press, Oxford, 1961.
- [50] R. Fu, G. Bodenhausen, *Chem. Phys. Lett.* 245 (1995) 415.
- [51] R. Fu, G. Bodenhausen, *J. Magn. Reson. A* 119 (1996) 129.
- [52] L. Frydman, T. Scherf, A. Lupulescu, *Proc. Natl. Acad. Sci. U.S.A.* 99 (2002) 15858.
- [53] J.-N. Dumez, L. Frydman, *J. Magn. Reson.* 226 (2013) 22.
- [54] E. Solomon, N. Shemesh, L. Frydman, *J. Magn. Reson.* 232 (2013) 76.
- [55] R. Schmidt, M. Mishkovsky, J.-N. Hyacinthe, N. Kunz, R. Gruetter, A. Comment, L. Frydman, *J. Magn. Reson.* 259 (2015) 199.
- [56] D. Idiyatullin, C. Corum, J.-Y. Park, M. Garwood, *J. Magn. Reson.* 181 (2006) 342.
- [57] J.-Y. Park, M. Garwood, *Magn. Reson. Med.* 61 (2009) 175.
- [58] R. Bhattacharyya, L. Frydman, *J. Chem. Phys.* 127 (2007) 194503.
- [59] K.J. Harris, A. Lupulescu, B.E.G. Lucier, L. Frydman, R.W. Schurko, *J. Magn. Reson.* 224 (2012) 38.
- [60] R.W. Schurko, *Acc. Chem. Res.* 46 (2013) 1985.
- [61] L.A. O'Dell, A.J. Rossini, R.W. Schurko, *Chem. Phys. Lett.* 468 (2009) 330.
- [62] L.A. O'Dell, R.W. Schurko, *Chem. Phys. Lett.* 464 (2008) 97.
- [63] L.A. O'Dell, R.W. Schurko, *J. Am. Chem. Soc.* 131 (2009) 6658.
- [64] A.W. MacGregor, L.A. O'Dell, R.W. Schurko, *J. Magn. Reson.* 208 (2011) 103.
- [65] K.J. Harris, S.L. Veinberg, C.R. Mireault, A. Lupulescu, L. Frydman, R.W. Schurko, *Chem. Eur. J.* 19 (2013) 16469.
- [66] R.W. Schurko, *Acc. Chem. Res.* 46 (2013) 1985.
- [67] B.E.G. Lucier, K.E. Johnston, W. Xu, J.C. Hanson, S.D. Senanayake, S. Yao, M.W. Bourassa, M. Srebro, J. Autschbach, R.W. Schurko, *J. Am. Chem. Soc.* 136 (2014) 1333.
- [68] S. Wi, Z. Gan, R.W. Schurko, L. Frydman, *J. Chem. Phys.* 142 (2015) 064201.
- [69] S. Wi, R.W. Schurko, L. Frydman, *J. Chem. Phys.* 146 (2017) 104201.
- [70] S. Wi, C. Kim, R.W. Schurko, L. Frydman, *J. Magn. Reson.* 277 (2017) 131.
- [71] M.M. Maricq, J.S. Waugh, *J. Chem. Phys.* 70 (1979) 3300.
- [72] A. Samoson, E. Kundla, E. Lippmaa, *J. Magn. Reson.* 49 (1982) 350.
- [73] K. Schmidt-Rohr, H.W. Spiess, *Multidimensional Solid State NMR and Polymers*, Academic Press, London, 1994.
- [74] M. Baldus, D. Rovnyak, R.G. Griffin, *J. Chem. Phys.* 112 (2000) 5902.
- [75] A.J. Vega, *J. Magn. Reson.* 96 (1992) 50.
- [76] A.J. Vega, *Solid State Nucl. Magn. Reson.* 1 (1992) 17.
- [77] K. Riedel, C. Herbst, J. Leppert, O. Ohlenschläger, M. Görlach, R. Ramachandran, *J. Biomol. NMR* 35 (2006) 275.
- [78] G. Kervern, G. Pintacuda, L. Emsley, *Chem. Phys. Lett.* 435 (2007) 157.
- [79] A.J. Pell, G. Kervern, L. Emsley, M. Deschamps, D. Massiot, P.J. Grandinetti, G. Pintacuda, *J. Chem. Phys.* 134 (2011) 024117.
- [80] R. Siegel, T.T. Nakashima, R.E. Wasylshen, *J. Magn. Reson.* 184 (2007) 85.
- [81] A.P.M. Kentgens, *J. Magn. Reson. A* 95 (1991) 619.
- [82] E. VanVeenendaal, B.H. Meier, A.P.M. Kentgens, *Mol. Phys.* 93 (1998) 195.
- [83] R. Bhattacharyya, L. Frydman, *J. Chem. Phys.* 127 (2007) 194503.
- [84] A. Gregorović, T. Apih, *J. Magn. Reson.* 233 (2013) 96.
- [85] U. Haeberlen, *Advances in Magnetic Resonance*, Academic Press, New York, 1976.
- [86] S. Vega, *J. Chem. Phys.* 68 (1978) 5518.
- [87] S. Vega, A. Pines, *J. Chem. Phys.* 66 (1977) 5624.
- [88] P.P. Man, in: D.M. Grant, R.K. Harris (Eds.), *Encyclopedia of Nuclear Magnetic Resonance*, J. Wiley, Chichester, 1996, p. p 3838.
- [89] A. Medek, J.S. Harwood, L. Frydman, *J. Am. Chem. Soc.* 117 (1995) 12779.
- [90] D.E. Demco, J. Tegenfelt, J.S. Waugh, *Phys. Rev. B* 11 (1975) 4133.
- [91] M.H. Levitt, *J. Chem. Phys.* 94 (1991) 30.
- [92] S.W. Ding, C.A. McDowell, *J. Magn. Reson.* 114 (1995) 80.
- [93] A.G. Redfield, *Phys. Rev.* 98 (1955) 1787.
- [94] Z. Gan, D.M. Grant, R.R. Ernst, *Chem. Phys. Lett.* 254 (1996) 349.
- [95] V.B. Cheng, H. Henry, J. Suzukawa, M. Wolfsberg, *J. Chem. Phys.* 59 (1973) 3992.
- [96] B.M. Fung, A.K. Khitrin, K. Ermolaev, *J. Magn. Reson.* 142 (2000) 97.
- [97] M. Ernst, A. Samoson, B.H. Meier, *J. Magn. Reson.* 163 (2003) 332.
- [98] R.K. Harris, G.J. Nesbitt, *J. Magn. Reson.* 78 (1988) 245.
- [99] M. Shen, B. Hu, O. Lafon, J. Trébosc, Q. Chen, J.-P. Amoureux, *J. Magn. Reson.* 223 (2012) 107.
- [100] F.G. Oas, R.G. Griffin, M.H. Levitt, *J. Chem. Phys.* 89 (1988) 692.
- [101] M.H. Levitt, T.G. Oas, R.G. Griffin, *Isr. J. Chem.* 28 (1988) 271.
- [102] Z. Gan, M. G. D, *Chem. Phys. Lett.* 168 (1990) 304.